ADVANCED ENERGY MATERIALS
www.advenergymat.de

Surface-Functionalized Nanoparticles as Catalysts for Artificial Photosynthesis

Gerard Martí, Laura Mallón, Nuria Romero, Laia Francàs, Roger Bofill, Karine Philippot, Jordi García-Antón,* and Xavier Sala**

Analogously to enzymatic catalysis, where the active metal sites and their environment are controlled by protein residues, the catalytic properties of metal nanoparticles (NPs) can be tuned by carefully selecting their surface-coordinated species. In artificial photosynthesis, surface-functionalization emerged in the last decade, grounded on the development of reliable methods for tailored synthesis, advanced characterization and theoretical modeling of metal NPs, altogether with the aim of transferring to the nanoscale the mechanistic knowledge acquired from molecular complexes. Metal NPs surface-functionalization modulates the energetics of key catalytic intermediates, introduces second coordination sphere effects, influences the catalyst-electrolyte interface, and determines the metal NPs surface coverage and, accordingly, the number of accessible active sites. In photoactivated systems, metal NPs surface-functionalization may play a key role in modulating the charge transfers and recombination processes between the light absorber and the active sites and in the light absorber itself. Thus, after a presentation of the most relevant synthetic methods to produce well-defined surface-functionalized metal NPs, a critical analysis of why the above effects are the cornerstone in enhancing their catalytic performance in the key processes of artificial photosynthesis, namely the oxygen evolution reaction, the hydrogen evolution reaction, and the CO_2 reduction reaction, is given.

1. Introduction

With a nanometric size (1–100 nm), metal-based nanoparticles (metal NPs) are greatly reputed for their unique properties compared to those of molecular metal complexes or bulk metals.[1–3] The quasicontinuous density of states present in bulk metals tends to a discrete energy level structure at the nanoscale due to the so-called quantum size effect.[1] Additionally, the richness of unsaturated (low-coordinated) atoms at NPs surface confers them peculiar reactivities with substrates.[2,3] Hence, metal NPs find diverse applications in the huge domain of catalysis,[4,5] including the fields of electrocatalysis[6–8] and photo(electro)catalysis,[9] two subareas to carefully explore in order to achieve a breakthrough in artificial photosynthesis. Apart from their matter state (finely divided metals) and their electronic properties, their reputation strongly relies on the fact that the smallest the size of a particle is, the higher the surface to volume ratio will be. This ratio is particularly high when metal NPs are around 1 nm in size or below (sub-nanoparticles), since the number of surface atoms can be > 90% thus providing a great number of potential surface-active sites. Determination of the number of atoms in the core and at the NP surface is possible by applying the rule of magic numbers that depend on the crystalline structure of the metal.[10] If very small metal NPs are in general amorphous, larger NPs can be more crystalline and expose atoms at their surface with different coordination numbers (owing to their location on the surface, namely corner, edge, and face atoms) that may induce different reactivities.[11] The reactivity of metal NPs is governed by the nature of their metallic core and their surface properties. The latter can be tuned to boost both reactivity and selectivity, enhancing the general performance of the nanocatalysts. This can be achieved by the functionalization of the NPs surface with appropriate capping agents, mostly by using small organic molecules (named as ligands).[12] The interaction of the ligands with the surface atoms of the NPs can be compared to ligand interactions with the metal centers in coordination complexes and metalloenzymes. Ligands can be chosen to tailor the surface properties of metal NPs through steric and/or electronic effects.[13]

G. Martí, L. Mallón, L. Francàs, R. Bofill, J. García-Antón, X. Sala
Departament de Química
Universitat Autònoma de Barcelona
Cerdanyola del Valles, 08193 Barcelona, Spain
E-mail: jordi.garciaanton@uab.es; xavier.sala@uab.cat
N. Romero, K. Philippot
CNRS
LCC (Laboratoire de Chimie de Coordination)
Université de Toulouse
UPR8241, UPS, INPT, F-31077 Toulouse cedex 4, France
E-mail: karine.philippot@lcc-toulouse.fr

The ORCID identification number(s) for the author(s) of this article can be found under https://doi.org/10.1002/aenm.202300282

DOI: 10.1002/aenm.202300282

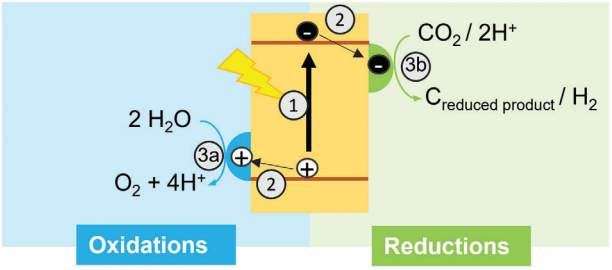

Figure 1. Schematic representation of the artificial photosynthesis process involving 1) light absorption, 2) charge separation, and 3) catalytic processes to produce oxygen in the oxidative side 3a) and reduced products in the reductive side 3b).

However, the functionalization of the NPs surface with a given ligand must be well-controlled to keep enough active sites. If introduced from the start of the synthesis, the ligand will act both as stabilizing and functionalization agent. Otherwise, it can be added in a second step (postfunctionalization, eventually performed via a ligand-exchange reaction) to decorate the NP surface.[12,14] A great variety of ligands can be used for the molecular surface-functionalization of NPs (amine, carbene, carboxylate, thiolate, phosphine, phosphonate, alkyne, polypyridyl, or porphyrin type ligands, etc.) depending on their nature, either metallic, metal oxides or quantum dots.[13] The coordinated ligands induce modification of the electronic spin density of the NP surface (electron-donor vs electron-withdrawing ligands; σ-donor vs π-acceptor ligands) that is of interest to study in order to adjust the NP performance in catalysis. Capping agent-stabilized metal NPs can be applied to catalysis as colloidal suspensions but also in heterogeneous conditions after their deposition onto a solid support. Precisely designed metal NPs (including the choice of an adequate and noninnocent capping ligand) are expected to present benefits from both homogeneous and heterogeneous catalysts, namely high reactivity, better selectivity, recyclability, and long-term stability.[15]

Metal NPs are a key element in the field of artificial photosynthesis (AP).[9] Mimicking the natural photosynthesis taking place in green plants and algae,[16] AP consists in storing sunlight energy into chemical bonds and is expected to be one of the key renewable energy technologies in the midterm. AP is a complex process (**Figure 1**) that starts with the absorption of light to generate separated charge carriers (electrons and holes), which are used by catalysts to generate fuels and/or chemicals. Usually, holes (oxidative equivalents) are consumed for oxidizing water to generate oxygen (Equation (1)), and the released electrons (reducing equivalents) allow to reduce protons to hydrogen (Equation (2)) or CO_2 to carbonaceous molecules, such as CO, methanol, ethanol, etc. (Equations (3a)–(3c))[17]

$$2H_2O \rightarrow 4H^+ + 4e^- + O_{2(g)} \quad (1)$$

$$2H^+ + 2e^- \rightarrow H_{2(g)} \quad (2)$$

$$CO_2 + 2H^+ + 2e^- \rightarrow CO_{(g)} + H_2O \quad (3a)$$

$$CO_2 + 6H^+ + 6e^- \rightarrow CH_3OH_{(aq)} + H_2O \quad (3b)$$

$$CO_2 + 12H^+ + 12e^- \rightarrow C_2H_5OH_{(aq)} + 3H_2O \quad (3c)$$

The oxygen evolution reaction (OER, Equation (1)) is a thermodynamically up-hill reaction ($E^0(H_2O/O_2) = 0.81$ V vs NHE at pH 7) of complex mechanism (removal of 4 H^+ and 4 e^- from two water molecules and formation of a new O—O bond) and slow kinetics.[18] Acting as the required electron source, the OER is a pervasive reaction in AP schemes and thus a key process in the production of solar fuels.[17] Both molecular complexes and metal oxides are interesting candidates to catalyze this reaction.[19] In general terms, molecular species are extremely fast and tunable, but relatively less robust.[20,21] In contrast, metal oxides are typically slow but more robust and easier to incorporate at the surface of (photo)electrode materials,[19] which place them closer to practical applications. The electrons supplied by the OER can then be employed in counterpart reduction reactions, such as the hydrogen evolution reaction (HER, Equation (2)) or the CO_2 reduction reaction (CO_2RR, examples in Equations (3a)–(3c)) to produce solar fuels and chemicals. HER is a less demanding ($E^0(H_2O/H_2) = -0.41$ V vs NHE at pH 7) two-electron reduction that needs to be catalyzed.[22] In this regard, Pt, with low working overpotentials and extremely high intrinsic activities (due to the ideal Pt–H adsorption energies), is still the metal of choice in acidic media for this reaction.[23] Nevertheless, Pt-based systems suffer from i) important corrosion under neutral/alkaline conditions[24] (where the OER is less energetically demanding), and ii) the prohibitive scarcity and price of the metal that prevents large-scale applications. On the other hand, CO_2 is a fully oxidized and thermodynamically stable molecule that can lead to multiple reduction products.[25] The key step in CO_2 conversion is the chemical transformation of this inert molecule into reduced carbon species, ranging from CO and HCOOH (2 e^- reduction) to 1-propanol (18 e^- reduction), passing through HCHO (4 e^- reduction), CH_3OH (6 e^- reduction), and ethylene/ethanol (12 e^- reduction). Nevertheless, the efficiency of the CO_2RR is typically hampered by i) the sluggish kinetics of the multielectron/multiproton processes that lead to high overpotentials (high energy costs) and low reaction rates, ii) the similar equilibrium potentials of the set of reductions listed above (e.g., ethylene, ethanol, and 1-propanol are all ≈0.1 V vs RHE), leading to product mixtures (high separation costs) in the absence of a highly selective catalyst, iii) the low solubility of CO_2 in aqueous electrolytes, and iv) the concomitant HER occurring at similar potentials.[26]

Different systems can be envisaged to combine these catalytic processes with appropriate light absorbers to produce solar fuels from AP, which can be grouped in two main categories: i) two-center systems, consisting in a photovoltaic device to generate green electricity connected to an electrolyzer, where the generated voltage is used to perform the chemical transformations, and ii) photoelectrochemical systems and particulate photocatalysts, where the light absorption, charge separation, and catalytic processes take place within the same particle or device (in a single material or in two separate materials, respectively).[27] From the catalytic point of view, the main difference between these two approaches is the source of charges: from an external circuit in the former and from the light absorber (consequently suffering from electron–hole recombination losses at the photoanode/catalyst/electrolyte interfaces) in the latter.[28] It is noteworthy that for both approaches, fast and efficient electrocatalysts toward each of the desired reactions are required.

Table 1. Comparison of the most relevant surface-functionalized OER electrocatalysts cited in this review. Parameters: mean diameter (Ø), onset overpotential (η_0, mV), overpotential at $|j| = 10$ mA cm^{-2} (η_{10}, mV), Tafel slope (b, mV dec^{-1}) and current density ($|j|$, mA cm^{-2}).

Entry	Catalyst	Electrolyte	Ø [nm]	Ligand/stabilizer	η_0 [mV]	η_{10} [mV]	b [mV dec^{-1}]	$\|j\|$[mA cm^{-2}][a)]	Refs.
1	Ir NPs	0.5 M H_2SO_4 (pH 0.3)	1.7 ± 0.3	4-ethylphenylacetylene	215	256	55	17 (270 mV)	[71]
2	Ir NPs	1 M KOH (pH 14)	1.7 ± 0.3	4-ethylphenylacetylene	265	300	37	20.9 (320 mV)	[71]
3	NiO NPs	1 M KOH (pH 14)	1–4	MeOPh	–	340[b)]	156	5.62 (450 mV)	[79]
4	NiO NPs	1 M KOH (pH 14)	1–4	None	–	315[b)]	133	6.85 (450 mV)	[79]
5	NiO NPs	1 M KOH (pH 14)	1–4	HCO_2—Ph	–	310[b)]	126	8.93 (450 mV)	[79]
6	NiO NPs	1 M KOH (pH 14)	1–4	Cl_2Ph—	–	293[b)]	129	13.17 (450 mV)	[79]
7	NiO NPs	1 M KOH (pH 14)	1–4	NO_2Ph—	–	287[b)]	89	18.98 (450 mV)	[79]
8	NiO NPs	1 M KOH (pH 14)	1–4	C_6F_5—	–	257[b)]	87	23.17 (450 mV)	[79]
9	$Co(OH)_2$ NPs	0.1 M NaOH (pH 13)	2.0 ± 0.5	Heptanol & carbon fibers (CFs)	322	–	176	–	[117]
10	$Co(OH)_2$ NPs	0.1 M NaOH (pH 13)	2.3 ± 0.5	Heptanol & COOH groups (oxidized CFs)	312	–	110	–	[117]

[a)] In brackets, overpotential at which the current density is registered; [b)] Overpotential at 1 mA cm^{-2} (η_1).

Table 2. Comparison of the most relevant surface-functionalized HER electrocatalysts cited in this review. Parameters: mean diameter (Ø), onset overpotential (η_0, mV), overpotential at $|j| = 10$ mA cm^{-2} (η_{10}, mV), Tafel slope (b, mV dec^{-1}), and current density ($|j|$, mA cm^{-2}).

Entry	Catalyst	Electrolyte	Ø [nm]	Ligand/stabilizer	η_0 [mV]	η_{10} [mV]	b [mV dec^{-1}]	$\|j\|$ [mA cm^{-2}][a)]	Refs.
1	Au NPs	0.5 M potassium phosphate (pH 6.7)	2.2 ± 0.4	porphyrin	330	460	101	4.8 (400 mV)	[70]
2	WSe_2 nanocrystals	0.5 M H_2SO_4 (pH 0.3)	–	Dodecylamine	365	540	110–155	1.8 (400 mV)	[72]
3	WSe_2 nanocrystals	0.5 M H_2SO_4 (pH 0.3)	–	None (after stripping)	247	422	88–121	7.7 (400 mV)	[72]
4	Ir NPs	0.5 M H_2SO_4 (pH 0.3)	1.7 ± 0.3	4-ethylphenylacetylene	20	43	26	14.9 (50 mV)	[71]
5	Ir NPs	1 M KOH (pH 14)	1.7 ± 0.3	4-ethylphenylacetylene	0	7	62	24.4 (50 mV)	[71]
7	Ru NPs	1 M H_2SO_4 (pH 0)	1.5 ± 0.3	4-phenylpyridine	0	20	29	0.55 (100 mV)[b)]	[76]
8	Ru NPs	1 M NaOH (pH 14)	1.5 ± 0.3	4-phenylpyridine	0	25	65	0.19 (100 mV) [b)]	[76]
9	Ru NPs	0.5 M H_2SO_4 (pH 0.3)	21.4	THF/MeOH	0	83	46	0.36 (100 mV) [b)]	[77]
10	CoP NPs	0.5 M Na_2SO_4 (pH 7.2)	12	Oleate	615	786	–	0.25 (500 mV)	[123]
11	CoP NPs	0.5 M Na_2SO_4 (pH 7.2)	12	Oleylamine	415	585	–	4.0 (500 mV)	[123]
12	CoP NPs	0.5 M Na_2SO_4 (pH 7.2)	12	Acetate	363	535	–	7.1 (500 mV)	[123]
13	CoP NPs	0.5 M Na_2SO_4 (pH 7.2)	12	None (after stripping)	360	532	–	7.5 (500 mV)	[123]
14	Au NPs	0.5 M H_2SO_4 (pH 0.3)	15	Citrate	120	270	74	60 (400 mV)	[122]

[a)] In brackets, overpotential at which the current density is registered; [b)] Specific current density ($|j_S|$, mA cm^{-2}).

Also, selective electrocatalysts are mandatory when a single carbon/multicarbon product is targeted from CO_2 electroreduction (Equations (3a)–(3c)), a rather unselective process. In here, metal NPs, which display high surface to volume ratio and tunable surface properties and are easy to deposit onto different supports, will have a pivotal role.

In the last decade, the access to efficient and reproducible synthetic methods to prepare well-defined metal NPs together with the interest in rationally tuning their reactivity to achieve efficient (highly active and selective) (photo)electrocatalysts for AP have pushed the emergence of innovative strategies for the NP surface-functionalization. This review presents a critical analysis of the most remarkable ligand-capped NP systems with the aim to shed light on the role of surface ligands in each case reaction: OER, HER, and CO_2RR. The manuscript is not intended to be comprehensive nor to provide a thorough numerical comparison of catalytic performances between the cases discussed. However, a summary of the main figures of merit for each electrocatalyst quoted along the discussion is given in Tables 1–3.

Given the key role of synthetic methods to produce well-defined surface-functionalized nanocatalysts, a dedicated section (Section 2) presents the main methods used to access such NP systems. Then, Section 3 debates on how surface-functionalization can directly affect the energy of the catalytic active sites and the catalytic intermediate species. How the capping ligands affect the NP-electrolyte interface by second coordination sphere and mass transport effects is covered in Section 4. Finally, Section 5 is dedicated to the role of NP surface functionalization in photocatalytic systems, where particular processes (i.e., light absorption, charge transfer processes) are key for the final catalytic output. Finally, a summary and future research directions are given in Section 6.

2. Synthetic Methods

Efficient synthetic methods that allow to have, in a reproducible manner, well-defined metal NPs (in terms of size, crystalline structure, metal core composition and stabilizing agents,

Table 3. Comparison of the most relevant surface-functionalized CO_2RR electrocatalysts performing in a two-compartment H cell (unless otherwise indicated). Parameters: mean diameter (Ø), potential (V, vs, RHE), CO (or C_{2+}, HCOOH, or C_2H_4) faradaic efficiency (%), CO (or C_{2+}), current density ($|j|$, mA cm^{-2}), CO (or total) mass activity (mA mg^{-1}), and CO turnover frequency (mmol cm^{-2} h^{-1}; s^{-1}, mmol g^{-1} h^{-1}, or molecules $site^{-1}$ s^{-1}). The electrolyte solution is a CO_2 saturated solution of: 0.1 M $KHCO_3$ (pH 6.8) A); 0.5 M $KHCO_3$ (pH 7.2) B); 1.0 M $KHCO_3$ (pH 7.8) C); 1.2 M $KHCO_3$ D); 0.1 M $NaHCO_3$ + 3.4 μM EDTA (pH 6.8) E).

Entry	Catalyst	Electro lyte	Ø [nm]	Ligand/stabilizer	Product [s]	Potential [V, vs RHE]	FE_{CO} [%]	$\|j\|_{CO}$ [mA cm^{-2}]	CO mass activity [mA mg^{-1}]	TOF_{CO} [rate]	Refs.
1	$[Au_{25}(PET)_{18}]^-$	A	–	2-phenylethanethiol	CO	−0.973	100	13	–	1.26 mmol cm^{-2} h^{-1}	[84]
2	Au/Cu NPs	A	1.5 ± 0.4	2-phenylethanethiol	CO	−0.80	100	2.9	500	–	[81]
3	Au NPs	B	4.2	Cysteamine	CO + H_2	−0.40	95.4	15	67.9	–	[86]
4	Au NPs	B	4.2	Ligand-free	CO + H_2	−0.40	25.0	0.5	0.6	–	[86]
5	Ag NPs	B	10	Cysteamine	CO + H_2	−0.60	93	1.9	4.01[a] (−0.5 V)	1.6 s^{-1}	[85]
6	Ag NPs	B	10	Ligand-free	CO + H_2	−0.60	10	0	–	0.03 s^{-1}	[85]
7	Ag NPs	B	5	Cysteamine	CO+ H_2	−0.75	79.2	4	40[a]	–	[82]
8	Ag NPs	B	4.9 ± 0.8	Oleylamine	CO + H_2	−0.75	92.6	–	37.5	–	[87]
9	Ag NPs	B	5.0 ± 1.0	Oleic acid	CO + H_2	−0.75	87.8	–	31.3	–	[87]
10	Ag NPs	B	4.9 ± 0.8	Dodecanethiol	CO + H_2	−0.75	65.2	–	62.5	–	[87]
11[	Au NPs	B	2.2	Oleylamine	CO + H_2	−0.80	93	5.8	–	22.2 s^{-1}	[83]
12	Au NPs	B	2.7	Ligand-free	CO + H_2	−0.80	71	2.4	–	7.7 s^{-1}	[83]
13	Au NPs	A	6.9 ± 0.8	*N*-heterocyclic carbene	CO + H_2	−0.57	83	2.3	–	–	[89]
14	Au NPs	A	6.9 ± 0.8	Ligand-free	CO + H_2	−0.57	53	0.4	–	–	[89]
15	Au NPs	A	14	Polydentate *N*-heterocyclic carbene	CO + H_2 (+ HCOOH)	−0.9	91	–	118[b]	–	[88]
16	Au NPs	A	14	Ligand-free	CO + H_2 (+ HCOOH)	−0.9	79	–	68[b]	–	[88]
17	Pd NPs	A	≈1–2	Polydentate *N*-heterocyclic carbene	CO + H_2 (+ HCOOH)	−1.26	62	–	1171[b]	–	[88]
18	Pd NPs	A	≈1–2	Ligand-free	CO + H_2 (+ HCOOH)	−1.26	40	–	1057[b]	–	[88]
19	Encapsulated Pd NPs[c]	C	2.5 ± 0.5	Bipyridine MOF (UiO-bpy)	CO + H_2 (+ HCOOH)	−0.80	98.2	4.2[d]	–	–	[92]
20	Encapsulated Pd NPs[c]	C	2.5 ± 0.6	Ligand-free MOF (UiO-67)	CO + H_2 (+ HCOOH)	−0.80	73.9	1.3[d]	–	–	[92]
21	Ag-Cu electrode	B	–	5-amino-1,3,4-thiadiazole-2-thiol (N_2SN)	C_{2+} + C_1 + H_2	−1.20	57.3[e] (C_{2+})	5.3[f] (C_{2+})	–	–	[96]
22	Ag-Cu electrode	B	–	Ligand-free	C_{2+} + C_1 + H_2	−1.20	18.3e) (C_{2+})	0.8[f] (C_{2+})	–	–	[96]
23	Ag-Cu electrode[g]	A	–	5-amino-1,3,4-thiadiazole-2-thiol (N_2SN)	C_{2+} + C_1 + H_2	−4.50[h]	79.9e) (C_{2+})	261[f] (C_{2+})	–	–	[96]
24	Ag-Cu electrodeg)	A	–	Ligand-free	C_{2+} + C_1 + H_2	−4.50[h]	30.9e) (C_{2+})	58[f] (C_{2+})	–	–	[96]

(*Continued*)

Table 3. (Continued).

Entry	Catalyst	Electro lyte	Ø [nm]	Ligand/stabilizer	Product [s]	Potential [V, vs RHE]	FE_{CO} [%]	$\|j\|_{CO}$ [mA cm^{-2}]	CO mass activity [mA mg^{-1}]	TOF_{CO} [rate]	Refs.
25	Cu NPs	A	50	Polyacrylic acid	CO + HCOOH + H_2 (+ CH_4 + C_2H_4)	−1.20	32.2 (CO) 37.6[i] (HCOOH)	6.3	–	–	[97]
26	Cu NPs	A	50	Polyvinylidene difluoride	CO + HCOOH + H_2 (+ CH_4 + C_2H_4)	−1.20	33.1 (CO) 21.1[i] (HCOOH)	5.7	–	–	[97]
27	Ag NPs[c]	A	12.1 ± 1.5	Oleylamine	CO + H_2 (+ HCOOH)	−1.10	29	0.049[d]	3.5	–	[120]
28	Ag NPs[c]	A	12.8 ± 1.6	1-methyl-3-*p*-nitrobenzyl imidazolium	CO + H_2 (+ HCOOH)	−1.10	74	0.258[d]	18.4	–	[120]
29	Ag NPs[c]	A	12.6 ± 1.5	1-octyl-3-*p*-nitrobenzyl imidazolium	CO + H_2 (+ HCOOH)	−1.10	92	0.256[d]	18.3	–	[120]
30	Ag NPs[c]	A	12.4 ± 1.4	1-hexadecyl-3-*p*-nitrobenzyl imidazolium	CO + H_2 (+ HCOOH)	−1.10	43	0.131[d]	9.4	–	[120]
31	Ag NPs[c]	A	12-13	1-triphenylmethyl-3- *p*-nitrobenzyl imidazolium	CO + H_2 (+ HCOOH)	−1.10	81	0.139[d]	9.9	–	[120]
32	Ag NPs[c]	A	12.6 ± 1.6	1-octyl-3-*p*-carboxybenzyl imidazolium	CO + H_2 (+ HCOOH)	−1.10	77	0.188[d]	13.4	–	[120]
33	Ag NPs[c]	A	12.6 ± 1.3	1-octyl-3-*p*-methylthiobenzyl imidazolium	CO + H_2 (+ HCOOH)	−1.10	77	0.160[d]	11.4	–	[120]
34	Cubic Cu nanocrystals[c]	D	44	1-octyl-3-*p*-nitrobenzyl imidazolium	C_2H_4 + HCOOH + CO + H_2	−50 mA cm^{-2}[j]	29.3[k] (C_2H_4) 19.0 (CO) 9.9[i] (HCOOH)	–	–	–	[119]
35	Cubic Cu nanocrystals[c]	D	36 ± 3	Ligand-free	C_2H_4 + HCOOH + CO + H_2	−50 mA cm^{-2}[j]	40.1[k] (C_2H_4) 19.0 (CO) 6.1[i] (HCOOH)	–	–	–	[119]
36	Spherical Cu nanocrystals	A	23.7 ± 1.1	1-octyl-3-*p*-nitrobenzyl imidazolium	H_2 (+ CO + CH_4 + C_2H_4 + HCOOH)	−1–10	75[l] (H_2) 3.7 (CO) 5.6[k] (C_2H_4) 7.4[i] (HCOOH)	–	–	–	[119]
37	Spherical Cu nanocrystals	A	23.7 ± 1.1	Ligand-free	H_2 (+ CO + CH_4 + C_2H_4 + HCOOH)	−1–10	60[l] (H_2) 7.4 (CO) 9.3[k] (C_2H_4) 7.4[i] (HCOOH)	–	–	–	[119]
38	Ag NPs	A	100 ± 20	Polyacrylamide	CO + H_2	−0.89	97.2	22.0	–	–	[118]
39	Ag NPs	A	100	Polymer-free	CO + H_2	−0.89	48.0	2.1	–	–	[118]
40	Au NPs	B	3.4 ± 0.5	Polyvinyl alcohol	CO + H_2	−0.58	97.0	43.8	260	–	[121]
41	Au NPs	B	3.4 ± 0.5	Polymer-free	CO + H_2	−0.58	53.0	13.4	–	–	[121]
42	CuO NPs	A	9 ± 2	Oleylamine	CO + H_2	−0.9	61	1.25[d]	26.2[a]	7.19 mmol g^{-1} h^{-1}	[126]

(*Continued*)

Table 3. (Continued).

Entry	Catalyst	Electro lyte	Ø [nm]	Ligand/stabilizer	Product [s]	Potential [V, vs RHE]	FE_{CO} [%]	$\lvert j\rvert_{CO}$ [mA cm^{-2}]	CO mass activity [mA mg^{-1}]	TOF_{CO} [rate]	Refs.
43	CuO NPs	A	5 ± 2	Ligand-free	CO + H_2	−0.9	47	0.11[d]	8.5[a]	1.02 mmol g^{-1} h^{-1}	[126]
44	Au NPs	A	2.4 ± 0.4	Oleylamine	CO + H_2	−0.7	75	6.3	217	–	[127]
45	Au NPs	A	2.4 ± 0.4	Propylamine	CO + H_2	−0.7	54	7.5	–	–	[127]
46	Au NPs	A	2.5 ± 0.5	Polyethyleneimine	CO + H_2	−0.7	23	1.3	–	–	[127]
47	Au NPs	A	2.4 ± 0.5	Ligand-free	CO + H_2	−0.7	52	5.7	193	–	[127]
48	Au NPs	E	2.0 ± 0.7	PPh_3	CO + H_2	−1.10	45	0.25[m]	–	–	[128]
49	Au NPs	E	2.1 ± 0.4	Dodecanethiol	CO + H_2	−1.10	37	0.81[m]	–	14 s^{-1}[n]	[128]
50	Au NPs	E	–	Ligand-free	CO + H_2	−1.10	64	1.14[m]	–	2.4 s^{-1}[n]	[128]
51	Au surface	E	–	Dodecanethiol	CO + H_2	−1.10	–	0.80[m]	–	–	[128]
52	Cu NPs	A	5.24 ± 0.71	Ligand-free	HCOOH + C_2H_4 + CO	−1.10	25.11[i] (HCOOH) 3.86[k] (C_2H_4) 2.78 (CO)	0.30[o]	–	–	[129]
53	Cu NPs	A	5.16 ± 0.74	Oleylamine	HCOOH + C_2H_4 + CO	−1.10	19.03[i] (HCOOH) 5.05k) (C_2H_4) 3.05 (CO)	0.37[o]	–	–	[129]
54	Cu NPs	A	5.25 ± 0.58	Tetradecylphosphonic acid	HCOOH + C_2H_4 + CO	−1.10	29.39[i] (HCOOH) 7.98[k] (C_2H_4) 5.01 (CO)	0.37[o]	–	–	[129]
55	Cu NPs	A	5.51 ± 0.60	Oleic acid	HCOOH + C_2H_4 + CO	−1.10	26.70[i] (HCOOH) 11.58[k] (C_2H_4) 4.31 (CO)	0.33[o]	–	–	[129]
56	Cu NPs	A	5.26 ± 0.55	Trioctylphosphine	HCOOH + C_2H_4 + CO	−1.10	32.63[i] (HCOOH) 2.39[k] (C_2H_4) 2.41 (CO)	0.35[o]	–	–	[129]
57	Cu NPs	A	4.87 ± 0.50	Dodecanethiol	HCOOH + C_2H_4 + CO	−1.10	13.33[i] (HCOOH) 0.16[k] (C_2H_4) 5.08 (CO)	0.15[o]	–	–	[129]
58	Ag NPs	A	30.2	Tetradecylphosphonic acid (NOLI)	CO + H_2	−0.68	86.6	0.93[d]	–	–	[131]
59	Ag NPs	A	30.2	NOLI-free	CO + H_2	−0.68	22.8	0.07[d]	–	–	[131]

[a] Total (CO+H_2) mass activity; [b] Total (CO+H_2+HCOOH) mass activity; [c] Measurements performed in a flow cell; [d] CO specific current density ($|j_s|_{CO}$); [e] C_{2+} FE (%); [f] C_{2+} specific current density ($|j_s|_{C2+}$); [g] Measurements performed in a flow cell (MEA flow electrolyzer) at a CO_2 flow of 10 cm^3 min^{-1} and a 0.1 M $KHCO_3$ flow of 30 mL min^{-1}; [h] Flow cell voltage; [i] HCOOH FE (%); [j] Fixed current density of the flow cell; [k] C_2H_4 FE (%); [l] H_2 FE (%); [m] Partial CO current intensity (mA); [n] TOF per active site; [o] Total specific current density ($|j_s|$).

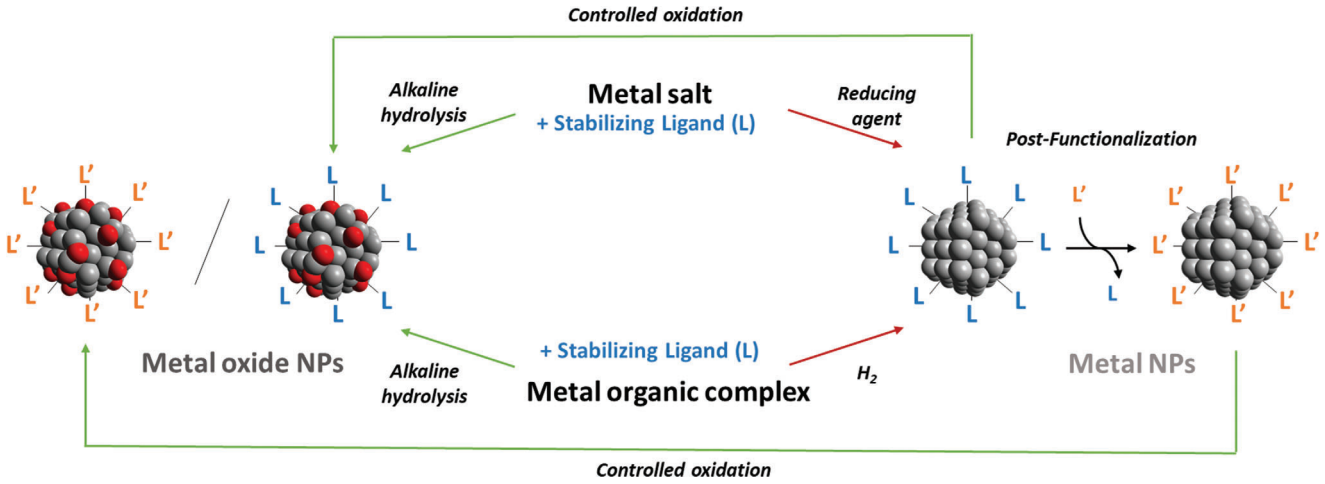

Figure 2. Schematic representation of the different synthetic approaches to obtain metal NPs (right, red lines) and metal oxide NPs (left, green lines). Metal atoms are shown in gray and oxygen atoms in red.

chemical order, shape, and dispersion)[29] are a prerequisite if one wants to finely investigate the catalytic properties of NPs and define the correlation between structural features and catalytic performance.[30] Different synthetic strategies have thus been developed (**Figure 2**), among which solution chemistry methods stand at a key position for their versatility, ease of use and more straightforward equipment than physical routes.[31] Liquid-phase methods are bottom-up approaches, meaning that the starting species contains one metallic atom that will lead to the formation of multiatomic metal species. Such starting species can be metallic salts[32] or metal–organic complexes.[33–36] The synthesis conditions (solvent, reducing agent, stabilizing agent, temperature, pressure, etc.) are adjusted depending on the nature of the metal source.

The reduction of a metal salt in aqueous media (Figure 2, upper right reaction) is a commonly used procedure to prepare metal NPs because of several advantages, including the low cost, ease of implementation, and scalability.[37] This method typically consists in treating an aqueous solution of a commercial metal salt by a reductant in the presence of a stabilizing agent, at ambient conditions or by heating, depending on the facility of reduction of the metal salt. Different reductants can be used for this purpose such as alcohols,[38] diols, or polyols,[39] hydrides such as $NaBH_4$,[40] surfactants like long alkylchain amines,[41] hydrazine,[31] or hydrogen gas under pressure,[33] among others. The synthesis of metal oxide NPs can be performed by coprecipitation from metal salts under basic conditions (NaOH) followed by a calcination step.[31] The role of the stabilizer is to avoid agglomeration of the NPs in solution and to control their growth (size and shape). They need to be water-soluble, among which organic polymers (like polyvinyl alcohol,[42] polyacrylamide,[43] polyvinylpyrrolidone,[44] surfactants like ammonium salts,[45] or ligands (i.e., citrate, amine, phosphine, thiols)[46] are commonly employed. By this way, long-term stable aqueous colloidal suspensions of NPs can be quickly obtained and directly used for catalysis in water without any purification. One disadvantage of this method is the possible presence of by-products resulting from the reactants (like halides), which can pollute the metal surface. Another inconvenient can be the (partial) oxidation of the metal surface, which is often circumvented by treating the colloidal suspension under hydrogen pressure before catalysis to, when needed, recover the metallic surface.[37]

Another method to form metal NPs consists in the reduction of a metal complex in an organic solvent (Figure 2, bottom right reaction). In particular, the organometallic approach is a well-established strategy to access well-defined metal NPs that can serve as model systems to explore the influence of the species present at their surface on the catalytic performance.[47] This synthetic method is based on the use of an organometallic complex (and in some extent a metal organic complex) as the source of metal atoms, together with an adequate stabilizer (various capping ligands can be used) that will govern the NPs growth. Apart from metal carbonyl precursors, which require high temperatures for the release of CO (solvothermal or hot injection methods), a clear advantage of using organometallic or metal–organic complexes is their easy decomposition under mild conditions (1–3 bar H_2; r. t. or $T \leq 423$ K) through reduction or ligand displacement from the metal coordination sphere in an organic solvent and in the presence of a given stabilizer. When available, olefinic complexes are preferred as precursors because they provide clean metal surfaces, as the treatment by H_2 releases alkanes that are inert toward the NP surface and easily evaporated. This enables to access metal NPs of ultrasmall size (≈1–10 nm) with a metallic surface free of contaminants, which can be tuned at will by the adequate choice of the capping ligand added as stabilizer. In addition, the stabilizer will functionalize the surface of the NPs, allowing thus to tune their surface properties with a positive influence on their catalytic performance.[48] By this way, monodisperse populations of metal NPs with an efficient control of size, shape, and surface state can be prepared. However, a drawback of this method may be the synthesis of the complex precursor, if not commercially available, and its handling, that may require high precaution (particularly when oxyphilic metals are used).

Supported metal NPs can be obtained by the two methods described above in a one-step[49–51] or two-step strategy.[52–54] If the support (carbon or graphene oxide material, metal oxide, MOF, etc.) is introduced in the reaction medium from the beginning of the synthesis protocol, the NPs will directly interact with the

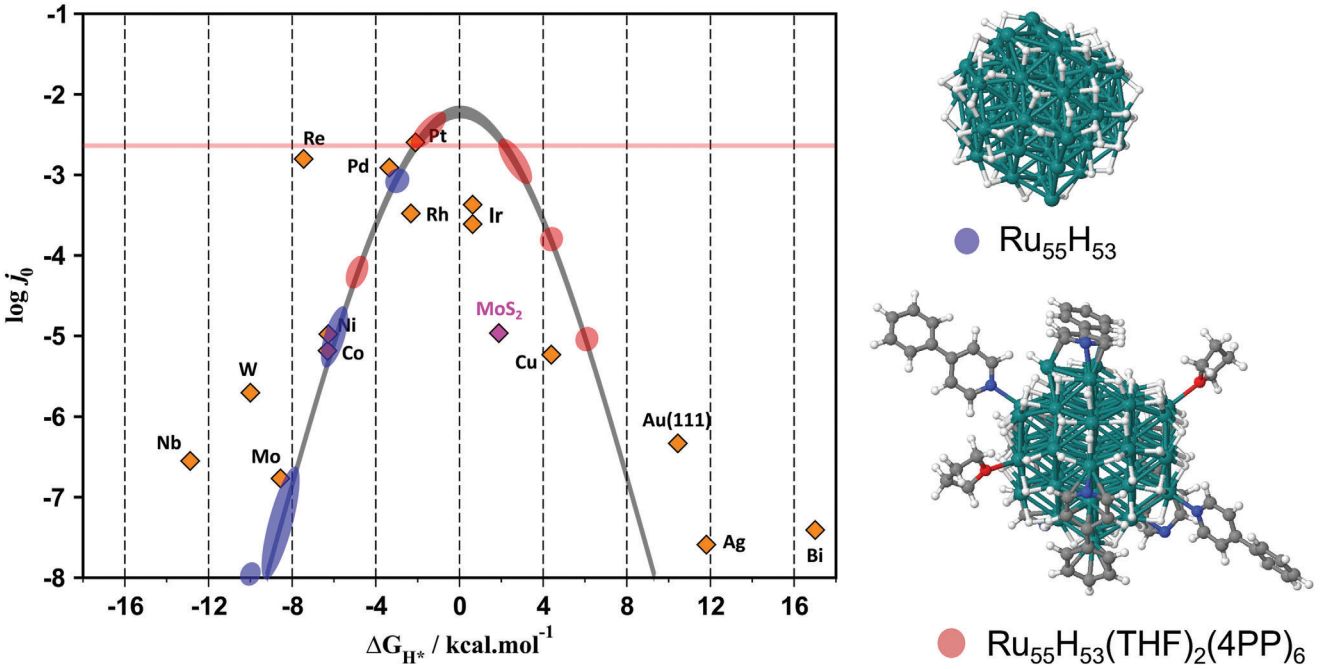

Figure 3. Volcano plot of the log of the experimental exchange current density j_0 (A cm^{-2}) versus the DFT- Gibbs free energy of H-adsorption, ΔG_{H^*}(kcal mol^{-1}), for pure metals[67] (orange diamonds) and nanoscale MoS_2 (pink diamond)[68] at acidic pH. The horizontal red line is the experimental $\log_{j0}$ value for Ru-4PP (4PP: 4-phenylpyridine). The results from our DFT calculations for ΔG_{H^*} in the different H probed sites for $Ru_{55}H_{53}$ (blue) and $Ru_{55}H_{53}(THF)_2(4PP)_6$ (red) are shown as oval shapes. Adapted with permission.[69] Copyright 2021, John Wiley and Sons.

support that can be eventually functionalized to increase the NP dispersion. Otherwise, the support can be impregnated by a colloidal suspension of preformed NPs. As for the capping ligand, the support can affect the reactivity of the NPs by electronic effects.

Concerning the synthesis of metal oxide NPs, it can be performed in one step conditions by alkaline hydrolysis of a metal salt[55] or an organometallic or metal–organic complex[36] in the presence of, for instance, a surfactant as stabilizer (Figure 2 left, green arrows). It can be also carried out via a two-step procedure by a controlled oxidation of preformed metal NPs (Figure 2, bottom green arrow from right to left).[56] As for the preparation of metal NPs, the reaction conditions are of paramount importance to get well controlled metal oxide NPs, and the choice of the capping ligand (present from the start synthesis or postadded) is also a key-parameter to have a tailored surface functionalization.

As it will become clear in the following sections, the catalytic properties of nanoscale materials are strongly affected by their surface chemistry. Thus, the tailored functionalization of the NP surface by the synthetic methods described in this section is an efficient strategy to boost their performance in both electrocatalysis and photocatalysis.

3. Electronic Effects in Electrocatalysis

Among the different roles capping species can play at the surface of metal NPs in electrocatalysis, the optimization of the binding of key reaction intermediates (i.e., *H, *OH, *CO, *COOH, etc.) by electronic modulation (resembling the electronic fine-tuning exerted by the coordination of donor or acceptor ligands in organometallic and coordination compounds) has been one of the most studied parameters. The following subsections summarize the main trends observed for electrocatalytic HER and OER (3.1) and CO_2RR (3.2).

3.1. HER and OER

The coordination of ligands at the surface of metal NPs is an efficient strategy to rationally fine-tune their HER activity. This strategy is related to the Sabatier principle (proposed by Paul Sabatier in 1911 based on empirical observations)[57] in heterogeneous catalysis and electrocatalysis[58] that predicts optimal activity on a catalytic surface with intermediate binding energies (or free energies of adsorption) for reactive intermediates. Therefore, the catalyst and the reactant will hardly interact if the bond between them is too weak, whereas a too strong bond will prevent reactant desorption and therefore will inhibit further reactions. More than a century later, it is now routine to evaluate in silico the binding energy of intermediate states by means of DFT methods,[59–62] recently aided by machine learning techniques to reduce computational costs.[63–65] In the case of HER, when the catalytic activity (exchange current density, log j_0) is plotted against the M—H bond strength (DFT-calculated Gibbs free energy of H-adsorption, ΔG_{H^*}), a volcano shape is obtained (**Figure 3**, left).[66] The tendency is inherent to metal or compound nature and only the catalytic systems laying on top of the volcano plot show optimal HER performances. However, surface-functionalization (i.e., ligand capping) can be used to adjust the hydrogen—metal bond strength to be neither too strong

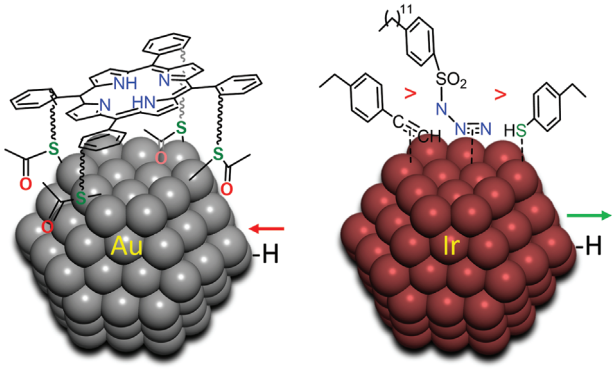

Figure 4. Face coordination of a porphyrin ligand on Au NPs strengthens the Au—H bond (left). Adapted with permission.[70] Copyright 2018. Royal Society of Chemistry. While 4-ethylphenylacetilene (EPA), 4-ethylphenylthiol (EPT), or 4-dodecylbenzenesulfonyl azide (DBSA) coordination on Ir NPs weaken the Ir—H bond (right). Adapted with permission.[71] Copyright 2021, American Chemical Society.

(avoiding poisoning of the surface) nor too weak (leading to a challenging activation) (i.e., $\Delta G_{H^*} \approx 0$), and thus rationally improve the HER activity. Some remarkable examples of this strategy are highlighted in this section.

For example, the Au—H bond is weak (it falls on the right part of the volcano plot, Figure 3). Therefore, strategies to strengthen the Au—H bond can lead to improved HER activity. Sakamoto, Teranishi and co-workers have proposed this beneficial strengthening of the M—H bond for the HER activity in porphyrin-modified Au nanoclusters (Au NCs) through an acetylthio bridge (CH_3—CO—S—, **Figure 4**, left).[70] Formation of Au—H* generates new bonding and antibonding states. Occupancy of the antibonding state determines the Au—H* strength. If the antibonding state is filled, the Au—H bond becomes weaker (and thus unfavorable for HER). On the contrary, a decrease in the antibonding state occupancy increases the M—H* strength. As observed by X-ray photoelectron spectroscopy (XPS) analysis, porphyrin coordination at the Au surface provokes a charge migration from the 5d state of the Au core to the Fermi level, which empties the antibonding state, thus improving its HER activity.

On the contrary, metals forming stronger M—H bonds that lay on the left branch of the volcano plot on Figure 3 (i.e., W or Mo, etc.) benefit from bond weakening strategies. In a sound example by Cossairt and co-workers, the HER performance of dodecylamine (DDA) stabilized WSe_2 nanocrystals is shown to improve after ligand stripping with Meerwein's reagent ($(Et_3O)(BF_4)$, entries 2 and 3 in Table 2), a universal alkylating reagent for native-ligand stripping of carboxylate-, phosphonate-, and amine-passivated nanocrystal thin films and dispersions to give bare or BF_4^-/DMF-passivated surfaces, an effect in part attributed to a decrease in ΔG_{H^*} to more favorable values.[72] As shown by ultraviolet photoelectron spectroscopy (UPS), DDA stripping populates more antibonding states, thus weakening the M—H bond and favoring the HER kinetics. The higher number of active sites available after ligand stripping also contributes to the higher HER activity, as will be discussed later in Section 4. Following the same trend, a recent report by Chen, Ping and co-workers describes the enhanced HER activity of 1.7 nm 4-ethylphenylacetylene-functionalized iridium NPs (Ir—C≡, Figure 4, right) when compared to commercial Ir NPs and analogous mercapto and nitrene surface-functionalized derivatives.[71] By combining experimental and computational data, the authors relate the M—H bond weakening (ultralow ΔG_{H^*} at the Ir—C≡ ligand anchoring sites) and the concomitant increase in HER activity of the Ir—C≡ system with the intraparticle charge delocalization induced by the conjugated interfacial Ir—C≡C— linkages, which allows more effective charge transfer from the Ir core to the surface ligands. Additionally, this intraparticle charge delocalization (yielding a low valent Ir surface, typically preferred for OER)[73,74] results key for the excellent OER activity of the Ir—C≡ system in alkaline media. During the rate determining step (rds), water molecules approach the Ir surface and dissociate into *H and *OH adsorbed intermediates in a vertical configuration onto two neighboring Ir atoms. Also, in this case the Ir—C≡ system exhibits the lowest energy barriers of all studied surface-functionalized Ir systems. Therefore, Ir—C≡-capping helps attending both a low Ir valence state by preventing further surface oxidation and a fast water dissociation process at the NP surface. The fine-tuning by ligand-capping of these key factors for OER kinetics may be transferred to other systems by a myriad of metal–ligand combinations. With remarkable catalytic properties in both HER (**Table 1**, entries 1 and 2) and OER (**Table 2**, entries 4 and 5), this Ir—C≡ system was implemented as a bifunctional catalyst in an overall water splitting device, working at low cell voltage in both acidic (1.473 V) and alkaline (1.495 V) media, outperforming commercial Ir/C.[71]

Interestingly, combination of experimental data with realistic computational models allowed to rationalize the effect of ligand-capping on the H-adsorption energy of Ru NPs at acidic pH. Based on a 1.0 nm 55-atom hcp Ru model NP,[75] the calculation of the binding energy for the different possible coordinating modes of a pyridine-based stabilizing ligand, namely the mono-*N*-dentate 4-phenylpyridine (4PP) ligand,[69,76] enabled to analyze its influence on the H-adsorption energies of the surrounding hydride ligands. In this atomistic model, the number of stabilizing ligands per Ru atom as well as the number of coordinating hydrides and tetrahydrofuran (THF) solvent molecules have been adjusted to the experimental ratios found (by combining inductively coupled plasma optical emission spectroscopy (ICP-OES), elemental analysis, thermogravimetric analysis, and hydride titration), in order to generate realistic models. DFT calculations indicate that the N-coordinating ligand shifts the H-adsorption energies from the left of the volcano plot (starting from the strong Ru—H bonds for bare Ru) to more balanced values, closer to the top of the volcano plot (Figure 3, oval shapes). This ligand effect on the H-adsorption energies (variation of the adsorption energies to approach the ideal 0 kcal mol^{-1}) is found to be transferred all over the NPs surface and is in accordance with the excellent HER electrocatalytic performance observed for the Ru-4PP system (Table 2, entry 7). Furthermore, DFT calculations proved that THF solvent molecules (with weakly coordinating character) exert lesser electronic influence than pyridine-based ligands, thus only slightly decreasing the Ru—H strength of the hydrides sitting at the same Ru site or nearby. This is in accordance with the worse electrocatalytic performance of THF/MeOH stabilized Ru NPs when studied in HER at acidic pH (Table 2, entry 9).[77] Ligand coordination modes (i.e., σ, π, or σ-π coordination of the 4-phenylpyridine ligand at the NP surface) and metal–ligand bond strengths have only been studied by

computational means (ligand adsorption energies).[76] Validation of these computational data by means of surface-sensitive characterization techniques (i.e., Time-of-Flight Secondary Ion Mass Spectrometry, ToF-SIMS,[78] and XPS) remains unexplored and would be of high interest, in particular if applied before and after catalytic turnover.

The potential of molecular surface-functionalization to optimize the OER activity of nanocatalysts has also been stablished in a sound example by Sun and co-workers. In this work, the local (surface) electronic structure of NiO NPs was adjusted and tailored by functionalizing their surface with different ligands. The postfunctionalization of ultrasmall (1–3 nm) NiO NPs with small organic molecules (MeOPh—, HCO_2Ph—, Cl_2Ph—, NO_2Ph—, and C_6F_5—) results on those bearing electron-withdrawing substituents (i.e., C_6F_5—) as the most active (both in terms of overpotentials and current densities, see Table 1, entries 3–8) in OER.[79] A combined electrochemical (CV, bulk electrolysis, electrochemical impedance spectroscopy (EIS)) and spectroscopic (XPS, X-ray absorption near edge structure (XANES), diffuse reflectance infrared fourier transform spectroscopy (DRIFTS), in operando Raman) analysis allows stablishing that electron-withdrawing ligands promote local electron-delocalization at the NiO surface, favoring the nucleophilic attack of water to the more electrophilic Ni centers. Furthermore, both Ni electrophilicity and the ability of the C_6F_5— group to promote proton shuttling aid the deprotonation in the required $Ni^{2+} \rightarrow$NiOOH reconstruction, thus also improving the OER performance of this system.

In summary, the electronic modulation of the NP surface by means of capping ligands has been extensively studied for HER (where the reaction conditions are less demanding and a good theoretical descriptor of the activity, ΔG_{H^*}, is available), but barely examined for the OER (where organic ligands may easily suffer from decomposition under the harsh oxidative environment required). In this line, molecular water oxidation catalysts can serve as inspiration to overcome this drawback at the nanoscale, given their well-stablished ligand design concepts.[20,80] Additionally, experimental determination of ligand coordination modes and binding strength through surface-sensitive characterization techniques (i.e., Time-of-Flight Secondary Ion Mass Spectrometry, ToF-SIMS,[78] and XPS) remains elusive.

3.2. CO_2RR

Concerning the CO_2RR, electronic modulation by molecular surface-functionalization has been mainly studied for Au NPs and Ag NPs ($2e^-$ CO-selective metals) in combination with carbene, amine, carboxylate, or thiolate ligands. Contrarily, the fine-tuning via ligand-capping of Earth-abundant metal-based nanocatalysts (i.e., Cu) able to yield more reduced high-energy density products from CO_2 (i.e., methanol, ethylene, ethanol, etc.) has been less explored.

Several examples of Au NPs or Ag NPs show that thiolate-based stabilizing ligands (2-phenylethanethiol (PET) or cysteamine (CA)) enhance the electroactivity for CO formation at the same time that increases the selectivity of the nanocatalysts with respect to HER.[81–86] A seminal example is the combined experimental and computational analysis of $[Au_{25}(PET)_{18}]^-$ clusters reported by Kauffman and co-workers (**Table 3**, entry 1). The anionic nature of the nanocatalysts promotes CO_2 adsorption and C═O bond activation by partial electron density donation from the S atoms of the shell to the O atoms of the adsorbed CO_2 molecules, thus polarizing the Au—S bonds and inducing electronic changes within the interior of the nanoclusters which bear resemblance to cluster oxidation.[84] At the same time, a proton capture and electron transfer convert adsorbed $*CO_2^-$ into adsorbed *COOH before evolving to CO and water. The same PET ligand used in bimetallic 1.5 nm Au/Cu NPs (49% Cu) also promotes CO selectivity (Table 2, entry 2).[81] Interestingly, DFT calculations on realistic models show how the thiol ligand properly stabilizes the *CO intermediate at the nanocluster surface and helps suppressing HER by disfavoring *H formation. Additionally, models with gradual ligand loss show a progressive increase of *CO stabilization that, eventually, hampers the proper desorption of CO, decreasing the overall CO selectivity of the system against HER. Analogously, similar electronic effects between the CA ligand and 4.2 nm Au NPs loaded onto carbon black have also been described. CA binding at the NPs surface results in decreased Au–Au coordination numbers (as confirmed by EXAFS) that create more vacancies and step sites, facilitating CO_2 reduction and thus mass activities up to 110 times higher than those of thiol-free identically sized Au–NP catalysts (Table 3, entries 3–4).[86] Likewise, the same CA ligand has been used to tailor the CO_2RR electroactivity of carbon-supported Ag NPs of different sizes (from 3 to 11 nm). DFT studies on bare and CA-stabilized models discard size effects as major contributor to the observed differences in electrocatalytic performance (Table 3, entries 5–7) but attribute them to a ligand-induced modification of the electronic spin density of the NPs surface. Thus, the breakup of the initial symmetry of the system upon thiolate ligand coordination provokes a progressive localization of the unpaired electrons at the surface of the NPs, which facilitates the stabilization of the key *COOH radical intermediate by providing more covalent character to the Ag—COOH bond.[82,85] In contrast, the localized unpaired electrons of the CA-stabilized system does not stabilize the Ag—CO donor–acceptor bond, thus facilitating CO desorption. This report is a sound example about how surface-functionalization by ligand-capping helps adjusting the stability of key CO_2RR intermediates to attain efficient (highly active and selective) electrocatalysts.

Additionally, advantageous effects provided by amine-based ligands with respect to thiolate ones for promoting effective CO selectivity have been demonstrated in a work by Kim and co-workers.[87] In this work, a comparison of the electrocatalytic CO_2RR activity of amine- (oleylamine (OLA); ethylenediamine, (EDA)), carboxylate- (oleic acid (OA)), and thiolate- (dodecanethiol (DDT), cysteamine (CA)) capped Ag NPs is presented (Table 3, entries 8–10). The higher CO selectivity of the amine-capped NPs is basically a consequence of their lower HER activity compared to the thiolate-based counterparts, which show much higher HER electrocatalytic activity but comparable CO mass activity, as also demonstrated by DFT calculations. As shown in **Figure 5**, amine-capped Ag NPs stabilize the *COOH intermediate while destabilize the *H one, whereas thiolate-capped NPs stabilize both intermediates, therefore not discriminating between HER and CO_2RR. On the other hand, carboxylate ligands stand in the middle (although closer to the amine ligands probably because of charge transfer from carboxylate to the Ag

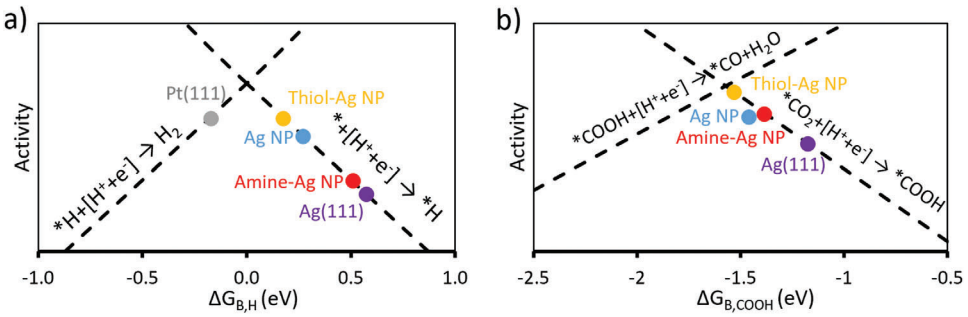

Figure 5. Volcano plots for a) HER and b) CO_2RR) of a Ag nanoparticle (Ag NP), a thiol-capped Ag NP, and an amine-capped Ag NP. The amine and thiol capping agents are propylamine and propane thiol, respectively. Dashed lines show the activities of each elementary step. Adapted with permission.[87] Copyright 2017, American Chemical Society.

NPs), showing intermediate HER and CO_2RR electrocatalytic activities.

The surface-functionalization of Au NPs[88,89] or nanoclusters[90] and Pd NPs[88] with strong sigma donating *N*-heterocyclic carbenes (NHC) has also been studied (Table 3, entries 13–18). As a general trend, NHC ligands favor CO production and stabilize the catalytic systems due to the formation of a strong M—C bond. Carbene coordination makes Au NPs surface highly electron rich, thus favoring their reductive capability, while at the same time destabilizing the bonds between adjacent Au atoms, which leads to a restructuration of the NPs surface and an increased number of defects that provide better kinetics for CO_2 reduction to CO.[89] As proposed by Yang and co-workers,[89] this may explain the drastic change in reaction mechanism between bare Au NPs and their NHC-capped analogues (Tafel slopes of 138 and 72 mV dec^{-1}, respectively) from a rate-determining step (rds) consisting in a single-electron transfer from $*CO_2$ to yield $*CO_2^{\cdot-}$ to a fast electron transfer to CO_2 before an rds chemical step.[89] Interestingly, the same change in reaction mechanism has been proposed for OLA-capped Au NPs deposited onto C nanotubes (CNTs), where the Tafel slope decreases from 252 mV dec^{-1} for the uncoated NPs to 78 mV dec^{-1} for the OLA-coated NPs (Table 3, entries 11–12).[83] In addition, NHC ligands have shown higher CO (vs H_2) selectivity in CO_2 electroreduction compared to thiol analogues in some examples. This is the case of the Pd NPs stabilized with polymeric NHC/thiol ligands reported by Liu and co-workers.[88] The cooperativity of the NHC electronic effects (increasing CO production vs HER activity due to strong σ-donation) and the hydrophobicity of the polymers (reducing the diffusion of the hydronium cation and binding to the NPs in a metalloenzyme-like behavior)[91] improve the Faradaic efficiency (FE) toward CO (Table 3, entries 15–18) and stabilize the systems against sintering under negative bias.[88]

The electron-modulation capacity of polypyridyl (2,2′-bipyridine (bpy)) surface species has also been reported in a recent work by Geng and co-workers on MOF (UiO-bpy)-encapsuled Pd NPs (Pd@UiO-bpy).[92] Combined in situ XRD (PdH_x phase analysis) and in situ Raman (*CO binding profiles) spectroscopies with DFT calculations on Pd@UiO-bpy and its bpy-free Pd@UiO-67 isomorph show how the electronic interaction of the bpy linker with the Pd surface optimizes the stability of key *H and *CO intermediates and thus the selectivity of the CO_2RR process. The electronic modulation exerted by the ligand allows suppressing the competing HCOOH formation at low overpotentials and evading the CO poisoning at high overpotentials, thus attaining FE over 80% for a wide potential range, from −0.3 to −1.2 V (vs RHE, Table 3, entries 19–20). This work highlights the interest of combining ligand-functionalized reticular materials with metal NPs in the field of CO_2 electroreduction, attaining high FE toward CO at remarkably low overpotentials (−0.3 V vs RHE, η = 200 mV).

Moving to Earth-abundant metals and more reduced products, Cu is the only reported metal able to catalyze the CO_2RR to high energy density multicarbon (C_{2+}) products (i.e., ethylene and ethanol) with reasonable FE. It is well-known that the selectivity and reaction rate toward C_{2+} products of Cu-based CO_2RR electrocatalysts increases as the average Cu oxidation state does.[93–95] In this regard, the first effective example of molecular surface-functionalization for this purpose has been reported recently.[96] Postfunctionalization of a micrometric tandem Ag—Cu electrocatalyst with electron-withdrawing aromatic heterocycles showed a threefold increase on the FE toward C_{2+} products of the electrode (Table 3, entries 21–24), attributed to the formation of $Cu^{\delta+}$ sites. The positive charge density of these $Cu^{\delta+}$ sites favors *CO adsorption and the concomitant formation of C—C bonds. However, the coordination mode of the surface ligands was not studied in detail. This report opens the avenue for the fine-tuning of Cu-based systems exploiting the myriad of possibilities offered by molecular surface-functionalization, particularly at the nanoscale. In this sense, a recent report from Park and co-workers on carbon-supported Cu NPs with polymeric stabilizers[97] highlights the key role of the functional groups (—COOH or —CF_2) of the binders used for the electrode fabrication, on the CO_2RR product distribution (Table 3, entries 25–26).

All in all, the interest in the electronic modulation of metal NPs in order to adjust the energetics of CO_2RR reaction intermediates to selectively attain a desired product is unarguable. This strategy has boosted the investigation of surface-functionalized nanocatalysts in the recent years. Most studies have been focused on $2e^-$ CO-selective metals (i.e., the precious Au or Ag). They have pinpointed thiol, amine, and carbene ligands as interesting surface-species to modulate *CO and *H adsorption energies and attain a decreased HER competition. Encouraging results have also been recently reported with surface-functionalized Cu systems, targeting C_{2+} products. To streamline catalyst design,

the introduction of multiscale[98–101] (i.e., microkinetic) modeling coupled to operando surface-sensitive techniques (i.e., time-resolved surface-enhanced Raman spectroscopy, TR-SERS[102]) to track the dynamics of reaction intermediates has proven useful in related systems[103,104] and will be of pivotal interest to disclose the effect of capping ligands in surface-functionalized nanocatalysts.

4. Electrolyte—NP Interface Effects in Electrocatalysis

In the last decades, the development of advanced electrocatalysts (including surface-functionalized NPs) and the understanding of mechanistic pathways to rationally design better catalytic systems have predominated. However, the study of the catalyst environment, where the catalyst–electrolyte interface can modulate key operational parameters such as reactant concentration, mass transport, proton delivery, intermediate stabilization, etc., is gaining more attention.[105,106] Accordingly, the following subsections focus on how NP surface-functionalization can affect and fine-tune the catalyst–electrolyte interface (i.e., by introducing steric hindrance, hydrophobic/hydrophilic character, stabilizing ions present in the electrolyte, etc.) through relevant examples. It is however worth to mention that the effects ligands provoke at the catalyst–electrolyte interface are often mixed and, therefore, it is not always straightforward to discriminate between them. This will be highlighted in the examples described hereafter.

4.1. Second Coordination Sphere Effects

Uncoordinated imidazole and carboxylate substituents in the amino acid residues of the protein backbone of photosystem II (PSII) are known to assist the oxygen-evolving complex (OEC), accelerating water oxidation during natural photosynthesis in plants and algae.[107,108] Similarly, amino acid residues are key for the enzymatic interconversion of CO_2 to either CO or formic acid[109] and the reversible conversion of protons and electrons to molecular hydrogen in [Fe–Fe]-hydrogenases.[110] Inspired by Nature, second coordination sphere effects have been transferred to synthetic molecular catalysts, resulting key for the exponential growth of reaction rates experienced in the last decade for reactions such as the OER,[111] HER,[112] and CO_2RR.[113] However, their implementation to nanocatalysis has been hampered by the intrinsically difficult characterization of surface-bound species, resulting in a lack of rationally designed catalysts at the nanoscale. Tailored NP surface-functionalization by the synthetic methods described in Section 2 coupled to operando characterization techniques pave the way to exploit second coordination sphere effects in nanocatalysis. However, examples are still scarce.

4.1.1. OER

Intramolecular second coordination sphere effects have shown to be key in lowering the activation energy at the rds when well-defined molecular complexes are used to catalyze the OER.[111] Combined experimental-computational works show how dangling basic substituents (i.e., carboxylate or phosphonate groups) act as proton transfer relays and accelerate the reaction kinetics.[114,115] Analogously to molecular complexes, the noncoordinated carboxylate groups present in a NiFe coordination polymer have been identified as dangling basic substituents able to act as proton transfer relays in heterogeneous surfaces, thus shuttling protons from the catalytic surface and accelerating the reaction kinetics.[116] At the NP scale, we have recently shown how carboxylates formed by the surface-oxidation of a carbon fiber (CF) likely act as proton acceptor moieties (internal bases) in a hybrid electrode, $Co(OH)_2$@CF, made of supported, 2 nm in size, $Co(OH)_2$ NPs. Carboxylate groups are suggested to lower the activation free energy that leads to O_2 formation during OER under alkaline conditions (Table 1, entries 9–10).[117] Unfortunately, the low metal loading in the carbon support prevented further experimental characterization of the active species and their dynamics. In the same vein, Sun and co-workers have recently reported on the proton transfer effects in the second coordination sphere of molecularly surface-functionalized 1–4 nm NiO NPs and their partial relationship (together with electronic modulation, see Section 3) with their outstanding OER performance (Table 1, entries 3–8).[79] Electron-withdrawing (C_6F_5—) aromatic ligands (in contrast to electron-donating (MeO)C_6H_4— ligands) show a specific proton affinity, which promotes proton shuttling, accelerating the deprotonation of $Ni(OH)_2$ in the formation of NiOOH, key intermediate species needed for effective O_2 evolution. In this case, operando Raman characterization under electrocatalytic conditions allowed to investigate the relationship between the nature of the capping ligands, the behavior of the active species and the observed electrocatalytic performance.

4.1.2. CO_2RR

Substituents in the second coordination sphere of surface-functionalized metal NPs have been shown to interact with CO_2 molecules, increasing the concentration and assisting the activation of this inert gas at the nanocatalyst surface, thus promoting both the activity and selectivity of the nanocatalysts in the CO_2RR. Functionalized Au and Ag NPs have been the systems of choice for these studies given the high activity and selectivity of these noble metals toward $2e^-$ reduced species (i.e., CO) and the relatively stable and well-known coordination chemistry at their surface.[85,86,118–121]

Two examples by Wang and co-workers[85,86] combining electrocatalytic techniques, operando ATR-IR spectroscopy and computational modeling, describe second coordination sphere effects for face-centered cubic crystalline Ag[85] and Au[86] NPs when stabilized with a self-assembled monolayer (SAM) of cysteamine (CA, **Figure 6**) coating ligand. The presence of dangling amine groups increases the CO_2RR activity toward CO evolution of the surface-functionalized nanocatalysts by increasing the reactivity of CO_2 molecules and suppressing the competitive HER (Table 3, entries 3–6). The —NH_2 groups form H bonds that stabilize chemisorbed CO_2 molecules at the NP surface and facilitate CO_2 activation (overpotentials decrease by ≈0.3 V). The so-assisted chemisorption of CO_2 is lost when the alkyl chain is elongated (because of geometrical constraints) or when a nonbind-

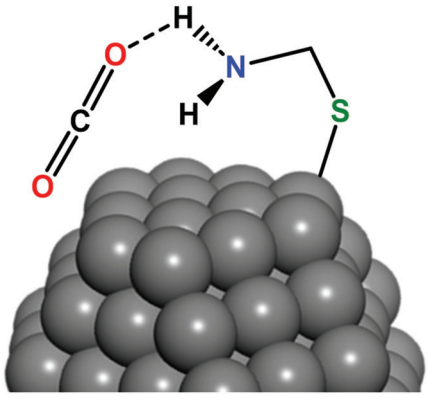

Figure 6. Representation of Cysteamine ligand on Ag or Au NPs interacting with CO_2 by H-bonding prior to chemisorption of CO_2 onto the NP surface. Adapted with permission.[85] Copyright 2018, American Chemical Society.

ing group replaces the amino terminal group. Other examples by Buonsanti and co-workers[119,120] describe the use of bridging imidazolium (IM) salts between an anchoring functionalized-phenyl group and an alkyl tail (see **Figure 7** in Section 4.2) in crystalline Ag NPs or in cubic Cu nanocrystals. In these studies, the electrostatic attraction between the positively charged IM and CO_2 helps the CO_2 approach to the surface of the catalysts, therefore increasing their activity toward the desired reduction product (CO for Ag NPs and formate for Cu NPs, Table 3, entries 27–35). However, steric hindrance also plays a crucial role in the selectivity toward CO, as it will be described in Section 4.2.

Stabilizing effect of second coordination sphere hydrogen bonds has also been described for polymeric stabilizers. Two representative examples have been reported by Niu and co-workers[118] and Zou and co-workers[121] for fcc crystalline Ag[118] and Au NPs[121] coated with polyacrylamide (PAM) and polyvinyl alcohol (PVA), respectively. In both cases, the hydrogen bonds formed between the amide NH_2 (PAM) or OH (PVA) functional groups and the O atoms of the CO_2 molecules facilitate their adsorption and allow the stabilization of the key *COOH intermediate formed before the evolution of CO, as demonstrated by DFT calculations and operando ATR-IR measurements.[118] This allows to increase both the selectivity and activity of the catalysts toward CO formation (Table 3, entries 38–41).

In summary, the works discussed in this section highlight the suitability of NP surface functionalization to induce second coordination sphere effects in electrocatalysis. Despite a still reduced number of examples, they show the capacity of bifunctional capping ligands to interact with the substrate molecules (i.e., CO_2, which is activated and concentrated at the NP surface) and reaction intermediates (for proton shuttling in the OER mechanism), thus positively impacting on the overall electrocatalytic output. Again, operando characterization techniques (i.e., ATR-IR) are key role to unravel the role of the capping ligand.

4.2. M—L Bond Strength and Mass Transfer Effects

The coordination capacity of the anchoring group determines the extent to which surface-active sites are blocked. Also, the chemical nature and volume of the ligand backbone influence the mass transfer (i.e., H^+/H_2O, CO_2, etc.) from the electrolyte to the catalyst surface by steric, electrostatic and/or hydrophobic/hydrophilic interactions. These effects are often mixed and not easy to distinguish for each metal–ligand combination. The following subsections, focused on HER and CO_2RR, intend to shed some light on the general trends observed.

4.2.1. HER

A survey of the literature in HER[72,122,123] shows that M–L combinations with moderate bond strength, low steric hindrance, and high proton affinity/hydrophilicity are desirable to maximize the HER activity.

Seminal examples can be found in the works of Cossairt and co-workers with surface-functionalized WSe_2[72] NPs and CoP[123] NPs. In both cases, ligand stripping with the Meerwein's reagent allows to examine the direct influence of ligand coverage on the HER activity. First, Wse_2 NPs were prepared using dodecylamine (DDA) as stabilizing ligand and compared with ligand-free NP counterparts (Table 2, entries 2–3).[72] Removal of DDA provoked only a modest increase in the surface area of the nanocatalyst (ECSA changes from 17.6 to 40.8 cm^2), but a clear decrease of its HER overpotential (by 118 mV). The authors explain the higher catalytic overpotential of the DDA-capped NPs as a combination of the steric hindrance inferred by the ligands, blocking the H^+/H_2O substrates to reach the active catalytic centers, and the detrimental electronic effect of the DDA ligands, which displace ΔG_{H^*} to negative values (see Section 3.1). Then, they studied the HER electroactivity of CoP NPs stabilized with carboxylate (acetate, octanoate, and oleate) and amine (oleylamine, octylamine, dioctylamine, trioctylamine, and butylamine) capping ligands following a similar methodology (Table 2, entries 10–13).[123] This study allowed assessing the effect of different M—L bond strengths and chain lengths in NPs of identical size. For the carboxylate-capped CoP system, the HER overpotential increases up to 250 mV from acetate to oleate, showing that surface ligands prevent catalysis by inhibiting the access of H^+/H_2O to surface active sites rather than poisoning them. If the latter were the case, all carboxylates would show similar activity regardless of the chain length. Interestingly, by using primary alkyl amines as capping ligands a different trend is observed, with constant HER overpotentials irrespective of the length of the alkyl chain. ECSA and thermogravimetric analysis (TGA) measurements explain this trend, showing lower ligand densities of amine ligands at the NPs surface compared to the carboxylate analogues. The lower ligand density, attributed to the weaker coordination capacity of oleylamine, eases the access of the substrate to the catalytic active sites. The quantitative analysis of ligand loading at the surface of identical size NPs is valuable and informative. When the data are combined with electrocatalytic benchmarking, it allows to stablish a meaningful comparison of the influence of the capping ligands employed.

Using the organometallic approach to synthesize metal NPs (see Section 2 for more details about this method), we have also provided examples where a moderate Ru—L bond strength, ensuring a high number of accessible surface sites while still benefitting from the electronic modulation exerted by the capping

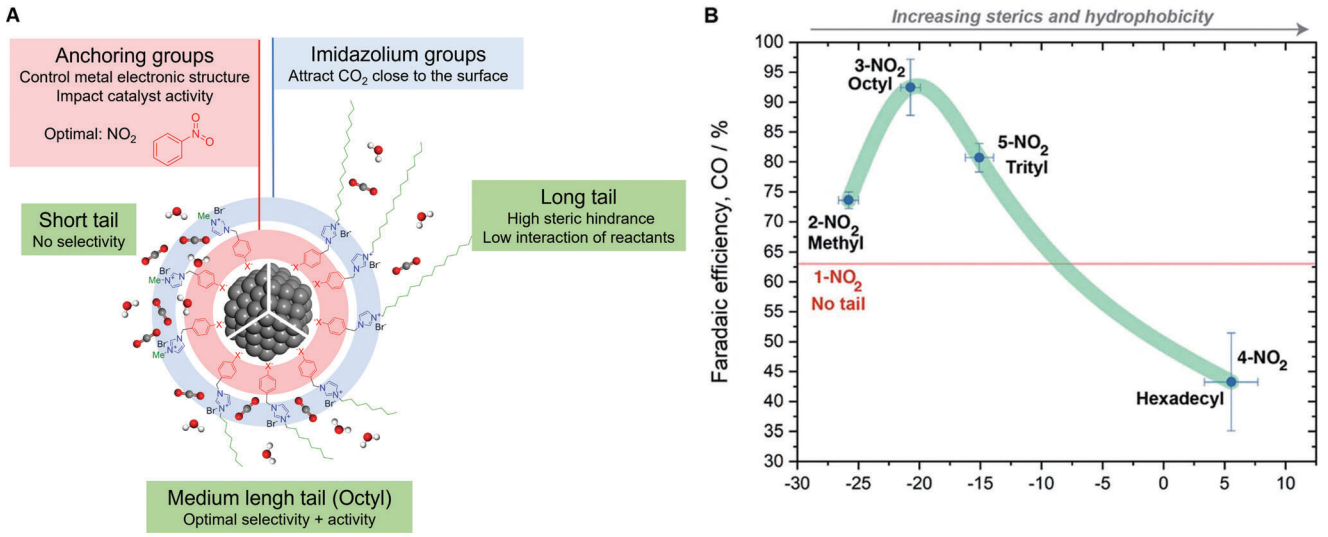

Figure 7. Surface-functionalized Ag nanocrystals with modular imidazolium ligands A) and graphical representation of the ligand alkyl chain properties versus attained Faradaic efficiency B). Adapted with permission.[120] Copyright 2019, Royal Society of Chemistry.

ligands (Section 3), is key for obtaining excellent HER electrocatalysts. A prominent example is the Ru4PP system, 1.5 nm Ru NPs stabilized by the 4-phenylpyridine (4PP) ligand.[76] This nanocatalyst shows excellent HER activity (η_{10} = 20 mV, Tafel slope (b) = 29 mV dec^{-1}) and clearly outperforms its "ligand-free" Ru-MeOH/THF counterpart (η_{10} = 83 mV, Tafel slope (b) = 46 mV dec^{-1}) prepared under identical conditions but with only MeOH and THF solvents as stabilizers (Table 2, entries 7 and 9).[77] The 4PP ligand provides a moderate ligand adsorption energy (DFT data) and appropriate electronic modulation (see Section 3), which leads to the outstanding HER activity.

The importance of a moderate M—L bond strength for attaining high HER electroactivity with surface-functionalized NPs is also highlighted in a work by Giner-Casares and co-workers about citrate-capped Au NPs.[122] The excellent performance of this nanocatalyst (Table 2, entry 14) is attributed to the weakly bonded citrate ligands, which efficiently stabilize the Au NPs while preserving enough free surface sites. Additionally, the work evidences the highly negative surface charge density induced by the ligand, increasing the number of hydronium (H_3O^+) ions at the electrochemical interface by an electrostatic interaction, thus decreasing the activation energy for HER electrocatalysis.

4.2.2. CO_2RR

In the last 5 years, the key role ligand-capping plays in tailoring the solid/liquid interface in CO_2 electroreduction, thus influencing both activity and selectivity, has become evident.[124–126] Reports on Au,[70,89,127,128] Ag,[87,120] and Cu-based[126,129] nanoscale electrocatalysts highlight how subtle is the balance between interwoven parameters, such as ligand coverage, M—L bond strength, steric hindrance, and hydrophilicity/hydrophobicity. The latter will be illustrated hereafter.

A report by Wang and co-workers[127] shows the benefits of coordinating a moderate amount of hydrophobic linear alkyl amines (propylamine, hexylamine, oleylamine, or ethylendiamine) at the surface of rGO-supported ultrasmall (≈2.4 nm) Au NPs (≈30% FE improvement toward CO formation vs the corresponding bare system; see Table 3, entries 44–47). According to DFT calculations on Ag NPs,[87] amine ligands improve CO selectivity versus H_2 evolution by adsorption at under-coordinated corner sites, which favor the stabilization of CO_2RR intermediates (*COOH) in the surrounding sites. Interestingly, Wang and co-workers[127] show that CO formation is hindered (thus promoting H_2 evolution) when bigger Au NPs (≈11.7 nm) are functionalized with alkylamines, or when the surface of the 2.4 nm Au NPs is functionalized with either a bulkier branched polyamine (polyethyleneimine) or linear alkylamines at higher surface coverage than the original system. Bigger NPs, with a lower proportion of undercoordinated sites for amine binding (favorable sites for *COOH stabilization) make the 11.7 nm Au NPs less CO selective, yielding similar FE for both bare and ligand-capped systems. The use of either amines with a higher density of anchoring groups (and thus stronger Au—ligand bonding) or a higher surface coverage of linear alkylamines depress CO formation through steric hindrance (obstructing CO_2 mass transfer) and/or the blocking of catalytic surface sites, decreasing the selectivity versus HER. The same inverse relationship between ligand bulkiness and CO selectivity has been described by Yang and co-workers when modulating the bulkiness of N-heterocyclic carbene (NHC) capping ligands at the surface of ≈7 nm Au NPs.[89]

Another sound example in which tailored ligand capping allows to fine-tune the solid/liquid interface in CO_2 electroreduction has been reported by Buonsanti and co-workers.[120] With Ag NPs as model catalysts, a family of modular imidazolium ligands with different functionalities (i.e., anchoring groups, alkyl chain length, Figure 7, left) have been studied to adjust the activity and selectivity of the resulting hybrid nanocatalysts toward the CO_2RR to CO (yielding FE up to 90%, Table 3, entries 27–33). As discussed in Section 4.1.2, the imidazolium group acts as a CO_2-capture motif, improving CO production by concentrating the reactant at the catalyst surface. The introduction of alkyl chains of different length onto the imidazolium scaffold affects

both the hydrophobic and steric properties of these surface ligands, thus impacting on both the intrinsic activity (j_{CO}) and the selectivity toward CO formation (FE, see Figure 7, right) of the nanocatalysts. As the tail length of the ligand increases, the permeability of both H^+/H_2O and CO_2 through the ligand shell decreases, thus lowering the overall activity of the catalytic systems. However, longer alkyl chains increase the hydrophobicity of the catalyst surface and disfavors HER in front of CO_2 electroreduction. An optimum situation is reached for medium-length alkyl tails (octyl chains, Figure 7, right). This work shows the importance of reaching a proper balance between ligand hydrophobicity and steric hindrance to attain surface-functionalized nanocatalysts able to selectively yield the desired CO_2RR products at relevant catalytic rates.

The above examples show that surface-functionalization is a proper way to fine-tune the CO_2RR properties of metal catalysts at the nanoscale, influencing the key figures of merit (activity, selectivity, and stability). Therefore, unravelling the fate of the employed ligands under turnover conditions is of outmost importance. Even if still relatively unexplored, some reports have recently tackled this challenge.[119,128–131] The encountered results are highly case sensitive (depending on numerous factors such as the M—L bond strength of the combined organic/inorganic components, the NPs size and morphology, etc.), but highlight the importance of a detailed study on the ligand fate and long-term role to rationally design improved electrocatalysts.

A first relevant example is the report by Baker and coworkers,[128] where the fate and role of dodecanethiol (DDT) at the surface of Au NPs (≈2 nm) for CO_2RR is studied in comparison with bare and PPh_3-caped Au NPs and DDT-capped flat Au surfaces (Table 3, entries 48–51). During the first minutes under negative potential, DDT partially desorbs from the Au NPs surface but remains at lower surface coverage at longer times. On the contrary, both DDT on flat Au surfaces (where the Au-DDT bond strength decreases) and PPh_3 on ≈2 nm Au NPs fully desorb under identical conditions. The long-alkyl chain ligand clearly improves the selectivity of the colloidal catalyst (presumably due to its hydrophobic nature) and enhances its stability against the deposition of poisoning cationic metals present in solution (i.e., trace Zn^{2+}). The corresponding bare Au systems (as-prepared or after PPh_3/DDT desorption via UV-generated ozone) are quickly poisoned under the same reaction conditions. Thus, DDT capping on small Au NPs forms a selective and durable molecular layer that allows CO_2 molecules to reach the catalyst surface but prevents surface poisoning by blocking the access of solvated Zn^{2+} cations, which are bigger in size (≈5 nm).

Buonsanti and co-workers have studied the fate of surface ligands on Cu nanocrystals (Cu NCs) and the correlation with the M—L bond strength[129] and the morphology[119] of the nanocrystals. In a first work,[129] Cu NCs (≈5 nm) were synthesized in the presence of trioctylamine and tetradecylphosphonic acid. Afterward, the stabilizing ligands were removed by treatment with the Meerwein's reagent and substituted by oleylamine (OLAM), oleic acid (OLAC), dodecanethiol (DDT), trioctylphosphine (TOP), trioctylphosphine oxide (TOPO), or tetradecylphosphonic acid (TDPA). Combined electrochemical analysis (Table 3, entries 52–57), surface characterization (XPS, EIS) and DFT calculations (metal–ligand bond enthalpies) allowed stablishing the M—L bond strength as a good predictive descriptor for the fate of the studied capping ligands under negative bias. Therefore, this seminal study allows classifying the used capping ligands (**Figure 8**) according to their labile (TOPO, OLAM, TDPA and OLAC), borderline (TOP) or nonlabile (DDT) character under turnover conditions. In the case of the Cu NCs studied in this work, the strongly coordinating and more persistent DDT ligand decreases the FE for CO_2RR products and shows the lowest intrinsic activity among all assayed ligands. On the contrary, labile ligands electrodesorb from the NCs surface under negative bias, showing comparable CO_2RR electroactivity to bare Cu NCs. These results are sound and pave the way toward a rational choice of the surface species according to the desired role (impacting or not the final catalytic output).

In another seminal work, Buonsanti and co-workers have shown the importance of the structural stability of the nanocatalysts when the surface-functionalization strategy is applied to improve the catalysis performance.[119] In imidazole-capped cubic (36 nm) Cu NCs, the imidazole ligand promotes CO_2RR over HER through electrostatic interactions with the CO_2 substrate and reaction intermediates (see Section 4.1 above). In contrast, spherical (24 nm) Cu NCs suffer from surface reconstruction under negative potentials, ejecting the surface ligands, thus losing the benefits of surface-functionalization (Table 3, entries 36–37). This work highlights the need of designing structurally stable catalytic systems by the appropriate M—L combinations.

The previous examples show that the electrodesorption of the NP capping ligands from the NP surface under the cathodic potentials required to drive the CO_2RR is a common phenomenon affecting their catalytic performance. However, Yang and coworkers[130,131] recently reported that the desorbed ligands can remain close to the NPs, order in a layer around them and still have a prominent impact on the electrocatalytic output. In this foundational work, a general evolution trend has been identified when using Au NPs or Ag NPs capped by long-chain ligands as CO_2RR electrocatalysts (under negative bias), which involves ligand decoordination followed by the formation of a NP/ordered-ligand interlayer (NOLI) state (**Figure 9**). The NOLI state acts as a durable (stabilized by intermolecular interactions between the decoordinated-physisorbed ligand chains in an enzyme-like mode) and specific (highly selective) catalytic pocket, which is preserved under negative applied bias and boosts CO production (by 2 orders of magnitude over bare NP systems; see Table 3, entries 58–59), disfavoring other competitive reactions (i.e., HER). Combination of electrochemical analysis (CV, bulk electrolysis), high-resolution microscopy (HR-SEM/TEM), and surface-sensitive spectroscopic techniques (XPS, SFG, EIS) allows the authors to explain the collective behavior of the NP surface ligands and the catalytic microenvironment responsible for the outstanding catalytic properties of the NOLI state. The potential transfer of this strategy to first-row transition metals has still to be mastered and will be a stimulating area of research in the near future.

In summary, the use of hydrophobic ligands (i.e., alkylamines) or surrounding ligand pockets (i.e., NOLI) has been proven to be beneficial to increase the selectivity toward CO_2 electroreduction products by impeding the diffusion of competing H^+/H_2O substrates to the NP surface.[88,120,127] However, caution must be taken with the bulkiness of the ligands[89,120,127] and the degree of surface coverage.[127] Both the use of branched/long alkyl chain

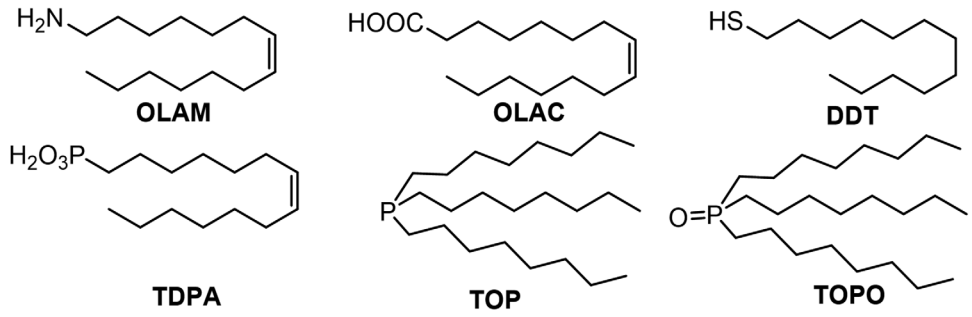

Figure 8. Ligands used by Buonsanti and co-workers.[129]

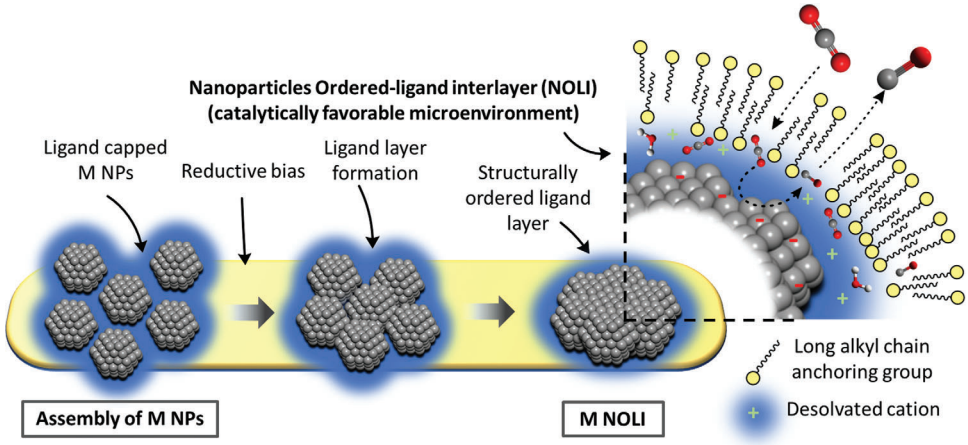

Figure 9. Generation of a NP/ordered-ligand interlayer (NOLI) state from ligand-capped NPs upon biassing under CO_2 electroreduction conditions (typical conditions: 0.1 M $KHCO_3$ saturated with 1 atm CO_2). Adapted with permission.[131] Copyright 2021, American Chemical Society.

ligands and high densities of ligands at the NP surface sterically prevent the CO_2 substrate to reach the metal active sites.

5. NPs Surface-Functionalization in Photo(electro)Catalysis

Metal-based NPs can be used in photo(electro)catalytic transformations as light absorbers (out of the scope of this review),[132] catalysts or photocatalysts (i.e., the NPs are able to both absorb light and drive the catalytic process).[133] In photo(electro)catalytic systems, the charge will be provided by the light absorbing unit upon light-driven charge separation. This is a complex process that starts with the excitation of one electron from the highest occupied level (HOMO for molecules, valence band for semiconductors) to the lowest unoccupied one (LUMO for molecules, conduction band for semiconductors). This only takes place when light of the appropriate energy (same or higher than the one between the two levels, the bandgap) is absorbed. Hence, the amount of absorbed light and the energy of the photogenerated charges will depend on the intrinsic optical properties of the light absorber. The photogenerated charges (excited electrons) can suffer from multiple recombination reactions (photogenerated charges that relax to their initial state). These processes can occur at different timescales depending on the nature of the recombination reaction:[134] i) ultrafast time scales, recombination between electrons and holes before being spatially separated; ii) micro to second timescales, recombination of spatially separated charges. These processes will strongly depend on the nature of the light absorbing unit, which can be a molecule, a metal coordination compound or a bulk semiconductor (inorganic, organic, or hybrid). In consequence, modulating all these charge transfer processes (accelerating the favorable ones and slowing down the unfavorable ones) is pivotal to deliver an efficient system.[135] In particular, the charge transfers between the light absorbing unit and the catalyst are of paramount importance and can be modulated by adjusting the interaction between these two components.[136]

Taking advantage of the surface functionalization of metal/metal oxide NPs, several strategies (**Figure 10**) have been used to design and modulate photo(electro)catalytic processes: i) dyad systems (Figure 10a), where the NPs are surface functionalized with a light absorber and combined with a sacrificial electron-donor/acceptor in photocatalysis; ii) photoelectrochemical systems based on dyad systems attached onto transparent semiconductors (Figure 10b); iii) photoelectrochemical systems based on the direct attachment of surface functionalized NPs onto a light-absorber semiconductor (Figure 10c). In all these strategies, the light absorption and the catalytic act take place at different parts of the photo(electro)catalytic system; the former at the light absorber (molecular dye or semiconductor material)

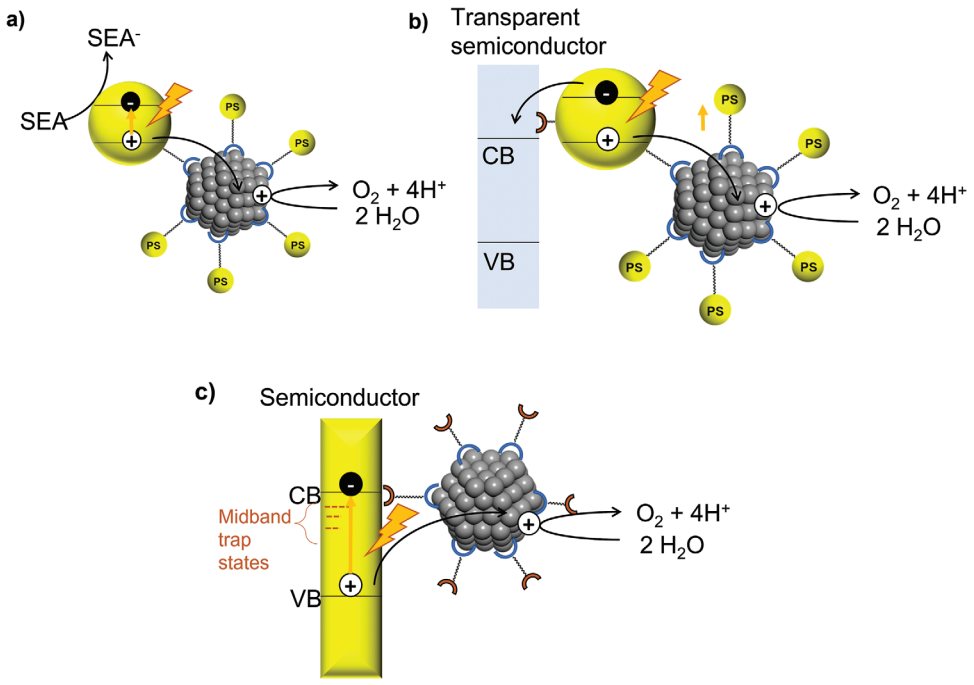

Figure 10. Schematic representation of three different strategies to use functionalized NPs in photocatalysis. All the energy levels are match for OER as an example. a) Dyad system, where the NP is functionalized with a molecular photosensitizer used in a three-component system. b) The dyad attached to a transparent semiconductor to be used as a photoelectrode. c) The NP is functionalized with molecules able to interact with a semiconductor which can directly absorb visible light. In the figure PS = photosensitizer, SEA = sacrificial electron acceptor; CB = conduction band; VB = valence band.

and the latter at the catalytic NP. This allows to spatially separate the photogenerated charges, slowing down the different recombination reactions and, at the same time, enhancing the kinetics of the desired catalytic process.[28] These strategies (Figure 10) are further discussed in the following subsections (5.1–5.4) and imply a major role of the NP surface ligands on the charge transfer processes between the light absorber and the nanocatalyst.

In contrast, other reports in photo(electro)catalysis describe surface functionalized NPs as mere catalysts, their main role being the use of the photogenerated charges to carry out the desired catalytic process. In this case, ligands can play similar roles to those described in electrocatalysis (Sections 3–4), affecting both the activity and the selectivity of the processes depending on the properties (i.e., hydrophobicity, bulkiness) and energetic modulation of the reaction intermediates exerted by the capping ligands. An example of this can be found in the work of Kim and co-workers on the gas-phase photocatalytic reduction of CO_2 by surface-functionalized Cu_2O–NPs with organic molecules (taurine (TAU) and ethylenediamine (EDA)) and deposited onto TiO_2.[137] This work shows how the ligand–metal interaction modulates the binding energy between the Cu sites and the key *COOH and *CO intermediates, thus determining the selectivity of the photogenerated products. NPs functionalized with an excess of TAU ligand present a higher selectivity toward CH_4 evolution than the corresponding EDA-functionalized ones, which preferentially produce CO. The weaker metal-CO interaction induced by the EDTA ligand promotes the evolution of this gas and hampers the attainment of further reduced products.

5.1. Dyad Formation

The dyad approach has been used for both HER and OER.[56,138–141] In all cases, a molecular metal complex-type photosensitizer (PS) is used to modify the nanocatalyst surface via the PS anchoring onto the NPs thanks to pending groups in the ligands of the complex. This modification allows the NPs to perform light driven reactions either using a sacrificial agent (Figure 10a) or being supported onto an electrode in a photoelectrochemical system (Figure 10b,c).

Following the first strategy (using a sacrificial agent), we have covalently grafted a molecular Ru PS ($[Ru(bpy)(bpyP2)_2]$, where $bpyP2H_2$ = P,P′-[2,2′-bipyridine]-4,4′-diylbis-phosphonic acid) at the surface of ≈3 nm prestabilized Co_3O_4 NPs (**Figure 11**), and tested the resulting hybrid dyad in the OER under photocatalytic conditions.[56] Interestingly, the separated counterparts (a physical mixture of PS and Co_3O_4 NPs) did not present any activity, highlighting the importance of their close proximity for the electron transfer to occur. In addition, in this work we have demonstrated that more PS units on the surface leads to a better performance due to the higher amount of photogenerated charges and the protection of the catalytic entity against aggregation.

A second example has been reported by Mallouk and co-workers. They prepared a wide family of IrO_2-$[Ru(bpyR_2)_3]$ ($bpyR_2H_2$ = 4,4″-dicarboxylic acid-2,2″-bipyridine (dcb) or 4,4″-diphosphonic acid-2,2″-bipyridine (dpbpy)) and IrO_2-$[Ru(bpyR_2)_2(bpyR'_2)]$ ($bpyR_2H_2$ = 4,4″-dicarboxylic acid-2,2′-bipyridine (dcb); $bpyR''_2$ = $[bpy(CONHSA)_2]^{4-}$ where $CONHSAH_2$ = 2,2″-[[2,2″-bipyridine]-4,4′-diylbis(carbonylimino)]bis-succinoic acid) dyads (see **Figure 12** for a drawing of a representative

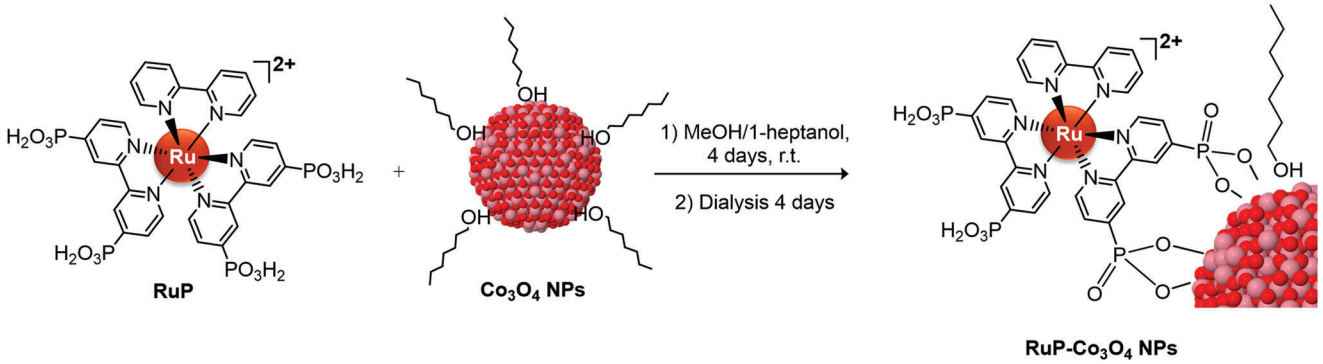

Figure 11. Scheme for the synthesis of Co_3O_4-[Ru(bpy)(bpyP2)$_2$] NPs. bpy = 2,2′-bipyridine; bpyP2 = 4,4″-bis(phosphonic acid)-2,2″-bipyridine. Adapted with permission.[56] Copyright 2018, Elsevier.

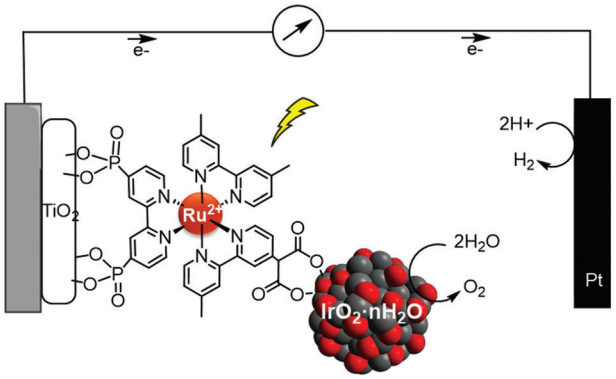

Figure 12. Schematic drawing of a photoelectrochemical OER device based on a TiO_2 photoanode doped with Ru-IrO_2 dyads and a Pt cathode. Adapted with permission.[141] Copyright 2009, American Chemical Society.

structure), and tested them as OER colloidal photocatalysts, reaching TONs up to 150.[139] Together with its role as light-harvester, the PS acts, in this case, as a stabilizing agent to obtain the desired NPs. In this regard, the authors highlight the benefits of carboxylate groups (vs phosphonate analogues) to stabilize IrO_2 NPs, better protecting the as-prepared dyads against aggregation.

Another work by Mallouk and co-workers[141] reports the use of similar RuPS-IrO_2 dyads supported onto the semiconductor TiO_2 as photoelectrodes. They prepared an heteroleptic Ru complex containing in one hand a bipyridine ligand bearing a phosphonate group to anchor the dye onto the TiO_2, and in second hand a bipyridine ligand with a carboxylate group to stabilize the IrO_2 NPs and anchor the molecular Ru-based PS onto their surface. Keeping the distance between dye and the TiO_2 and the IrO_2 NPs minimal resulted in a functional photoanode (Figure 12).

The main drawback of this system resulted to be the slow electron transfer between the dye and IrO_2, as demonstrated using transient absorption spectroscopy (TAS). As will be discussed in the next subsection, this can be adjusted by modulating the redox potentials of the dye or tuning the electron transfer by changing the distances between the different components of the system. A more recent example by Tran and co-workers reports a photoanode based on the covalent anchoring of a phosphonated Ru-phenanthroline PS onto Fe@FeO_x core/shell NPs and the deposition of this dyad onto a fluorine doped tin oxide (FTO) support.[138] The system showed to outperform, both in terms of activity and stability, the OER performance of the photoelectrode counterpart made of a physical mixture of PS and Fe@FeO_x NPs. No TAS data are reported in this case, and thus the origin of the observed charge recombination remains unclear.

All in all, dyad formation seems to be a convenient approach to improve the performance of OER photoanodes. However, charge transfer analysis is frequently hampered by the low dye loadings at the NPs surface and light scattering, thus hindering the rational fine tuning of the photoelectrodes prepared by this strategy.

5.2. Modulation of the Electron Transfer

In a photo(electro)catalytic system, a key factor to attain a high performance is to have an efficient charge transfer between the light harvesting unit and the nanocatalyst. This can be tuned by rationally designing the ligand to modulate the distance[141] and the electronic coupling, or by changing the energetic levels to make them more favorable. The following are representative examples of this strategy.

TiO_2 photoanodes codoped with phosphonate-derived $[Ru(bpy)_3]^{2+}$ and IrO_2 NPs functionalized with a PSII tyrosine-histidine mediator mimic (**Figure 13**) have been found to oxidize water with double the quantum yield as their nonfunctionalized counterparts.[55] Mallouk and co-workers proved, using flash photolysis, that this improvement is due to the improved electron transfer between the dye and the catalyst.

Also, surface-functionalization of myristic acid-stabilized MnO NPs with different capping agents has been reported to tune the OER activity of a WO_3/$BiVO_4$-MnO hybrid photoanode.[142] This work by Nam and co-workers relates the nature of the exchange species at the interface with changes in the band edge energetic level of the MnO NPs. Surface BF_4^- anions were found to lower this energetic level (using UPS measurements), facilitating the hole transfer from the WO_3/$BiVO_4$ light harvesting unit, resulting in enhanced charge separation efficiency and OER performance. The opposite trend (increasing the energetic levels, and thus disfavoring the charge transfer from the $BiVO_4$ to the MnO NPs) was observed when a Ca^{2+}-EDTA complex was used as NP stabilizer.

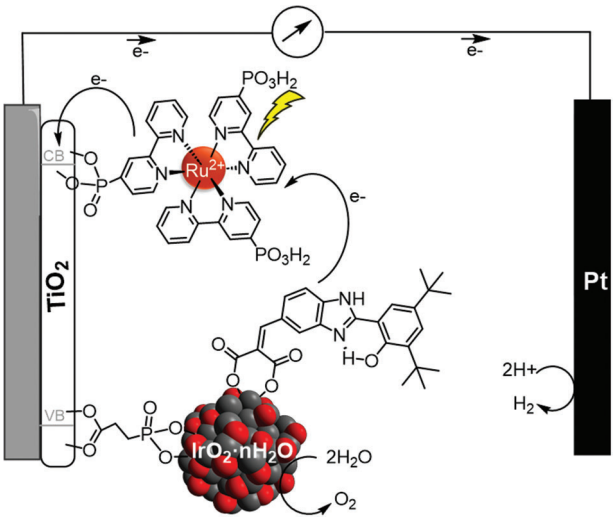

Figure 13. Schematic drawing of a photoelectrochemical OER device based on TiO_2 photoanodes codoped with phosphonate-derived $[Ru(bpy)_3]^{2+}$ and IrO_2 NPs functionalized with a PSII tyrosine-histidine mediator mimic. Adapted with permission.[55] Copyright 2012, PNAS.

5.3. Passivation of the Semiconductor Mid Bandgap States

The passivation of mid bandgap states approach is only applicable when the nanocatalyst is deposited/attached onto a semiconductor material (Figure 10c). Usually, the semiconductor presents mid bandgap defect states (inherent to most semiconductors due to the presence of intrinsic defects) that can act as recombination sites, thus lowering the charge separation efficiency and consequently their final performance. The presence of stabilizers onto the semiconductor surface can alter the concentration and energetics of these trap states. This effect has been widely studied in quantum dots, where surface-functionalization can modulate the trap states, enhancing charge separation and consequently leading to higher quantum yields in photocatalysis.[143–145]

5.4. Combined Approach

A recent report by Wang and co-workers[146] on a WO_3-CoO_x photoanode discusses the role of 3,3-diphosphonopropanate used as the ligand to stabilize the CoO_x nanocatalyst considering the three approaches (5.1–5.3) described above. First, ligand coordination at the NPs surface stabilizes the formed CoO_x nanocatalyst (approach 5.1). Second, similar to examples described in approach 5.2, the ligand is shown to be the responsible for the fast and efficient charge transfer from WO_3 to the CoO_x nanocatalyst. Additionally, the 3,3-diphosphonopropanate ligand acts as a spacer between WO_3 and CoO_x, slowing down the recombination processes. Finally, the presence of this ligand on WO_3 was demonstrated to increase the photogenerated charge, which was associated with the decrease of the intrinsic WO_3 trap states (approach 5.3).

In summary, when examining the role of surface ligands in photo(electro)catalytic systems based on surface-functionalized NPs, the following parameters need to be considered:

1) The ability of the ligand to stabilize the metal NP under turnover conditions (i.e., preventing aggregation or sintering, improving the dispersibility, etc.).[56,137,139,140]
2) The capacity of the ligand to modify the binding energy of reaction intermediates or the redox surface chemistry of the NPs, having a similar role as in electrocatalysis. However, care must be taken here when moving from electro- to photo(electro)catalysis. In a photoactivated system, the NP energy levels need to be well aligned with those of the light harvesting unit (the electron transfer needs to be possible, and therefore the electron needs to be transferred from a higher energetic level to a lower one).[137,142]
3) The ability of the ligand (according to its chemical nature[55,56,141] and length[146]) to modulate the electron transfer rates (both forward and backward) between the catalyst and the light harvesting unit, potentially lowering down charge recombination and allowing higher charge accumulation onto the catalyst.
4) The impact of the organic ligands in the light harvesting unit. As shown in the case of semiconductors, surface-functionalizing molecules can modulate the presence of trap states, yielding more efficient charge separation.[146]

All the above interrelated aspects should be judiciously considered when designing, characterizing and testing photo(electro)catalytic systems based on surface functionalized NPs as catalysts. The examples in this section highlight the potential of surface-functionalization as a tool for the design of tailored photoelectrodes with enhanced performance. Unfortunately, the still short number of systems reported to date (and thus the reduced photophysical data available to correlate the nature of the catalysts with their properties/activity) combined with the lack of standard benchmarking protocols in the photo(electro)catalysis field[147,148] (difficulting the analysis of the results) hampers the extraction of solid guidelines to rationally design improved systems.

6. Conclusion and Outlook

The surface-functionalization strategy has recently arisen as a promising and powerful approach to fine-tune the catalytic capacity of metal NPs in AP. The field has evolved fast in the last decade thanks to the mechanistic understanding acquired from the study of molecular species, which can be partially transferred to the nanoscale, along with the development of reproducible methods for the tailored synthesis of NPs and also of advanced techniques for their characterization and modeling. The large variety of coordinating species (i.e., ligands) offers limitless combinations with the inexhaustible pool of metal/metal oxide mono- or multimetallic NPs, ensuring access to a myriad of surface-functionalized systems of assorted catalytic properties.

By now, the surface-functionalization strategy has been applied mostly for the reductive processes of AP, namely HER and CO_2RR, leaving the oxidation counter reaction (the OER) mainly unexplored. Indeed, for the OER, only a few reports highlight the beneficial role of i) carboxylate ligands at the NP second coordination sphere that boosts the reaction kinetics via proton shuttling, and ii) electron-delocalization induced by ligand capping, that enhances the reaction kinetics by favoring the nucleophilic attack

of water. The low implementation of surface-functionalization strategies for the OER may result from the harsh oxidative conditions in this reaction, which may compromise the stability of the carbon-based capping ligands.

Surface-functionalized NP-based HER catalytic systems have been more explored. The hydrogen adsorption energy is a well-known descriptor to explain/predict the HER activity of a given metal toward this reaction, which should be neither too high nor too low to favor both the adsorption and desorption steps. The examples in Section 3 show how the control over the electronic effects exerted by the ligands is the cornerstone to achieve balanced hydrogen adsorption energies and, consequently, excellent catalytic activities. These examples also highlight the importance of building realistic theoretical models based on experimental data from spectroscopical, analytical, and electrochemical characterization to better understand the correlation between ligand coordination and catalytic performance. This experimental-computational approach will allow to consider relevant properties of the ligands such as their density, bulkiness, coordination ability, electronic influence, etc., enabling the rational design of ligand-functionalized HER nanocatalysts.

The inherently complex selectivity of the CO_2RR (among CO_2-derived products and vs the concomitant HER in aqueous media) makes the development of NP surface-functionalization strategies still more appealing. However, the mixed effects of the surface ligands (see Sections 3–5), all of them key on determining the final catalytic output, make the rational design of efficient nanocatalysts via ligand-surface engineering still a great challenge. Nevertheless, sound breakthroughs have been made, for instance, in the electronic modulation of the key reaction intermediates (i.e., *CO, *COOH, *H, etc.), whose stabilization/destabilization dictate the final selectivity of the nanocatalysts. In this regard, due to a well-known surface coordination chemistry and high selectivity for $2e^-$-reduced products, noble metal (Au, Ag)-based systems dominate most studies and represent good model systems for more complex endeavors, encompassing Earth-abundant metals and more reduced products. About the latter, the electronic modulation of Cu NPs with the appropriate capping ligands have shown increased selectivity to high-energy density C_{2+} products (see Section 3). Recently, Ni catalysts bearing $Ni^{\delta+}$ surface sites have been reported to have a similar reactivity for the first time.[149] Similar to the Cu case, favoring $Ni^{\delta+}$ states by the appropriate capping ligands is a promising approach to efficiently produce C_{n+} products from CO_2 on catalysts based on Earth-abundant metals. Relevant advances have also been made in suppressing the parasitic HER by the engineering of the NP-electrolyte interface. For instance, second coordination sphere effects have shown to increase the local surface concentration of the CO_2 substrate and assist its activation. Also, the proper balance between ligand hydrophobicity and steric hindrance has shown to be key on determining the nanocatalyst activity and selectivity toward the desired products at a relevant catalytic rate. For example, the use of hydrophobic ligands (i.e., alkylamines) improves the selectivity toward the CO_2RR by impeding the diffusion of the competing H^+/H_2O substrates for HER. However, a high surface coverage with bulky ligands (branched/long alkyl chains) prevents the diffusion of the CO_2 substrate toward the NPs active sites, thus hampering the catalytic reaction. Besides the steric volume of the ligand, the surface covered by the capping ligands also relies with the M—L bond strength. Moderate values of the latter are more favorable due to the good balance between NPs stabilization and the number of available surface-active sites. Finally, depicting the nanocatalyst structural stability/evolution under operational conditions (structural changes can lead to the total/partial ejection of surface ligands) is pivotal to understand and predict the fate of surface ligands along the reaction and thus to rationally design surface-functionalized NP systems of practical application. For instance, ligand ejection has shown to be beneficial in certain cases for CO_2RR, with the formation of NP-ordered ligand interlayer (NOLI) systems such as those described at the end of Section 4.2.

Photoactivated surface-functionalized systems present some additional characteristics that need to be considered to rationally design more efficient catalysts. The charge transfer between the light absorber and the nanocatalyst and the recombination processes (which impact on the system photo(electro)catalytic performance) can be optimized by changing the nature/length of the ligand/linker between them. For example, medium length ligands are optimum, providing efficient charge transfer to the nanocatalyst, while slowing down undesired recombination processes. Additionally, when semiconductors are used as light absorbers, the presence of capping ligands at the nanocatalyst surface can tune the quantity of trap states (usually responsible for recombination processes), yielding more efficient charge separation.

The examples discussed in this review demonstrate that using ligands to functionalize the surface of metal NPs may strongly affect the final performance (both in terms of kinetics and selectivity) in electro- and photocatalysis. This opens new avenues to rationally fine tune the selectivity and activity of metal NPs for different redox reactions, an analogous strategy to that followed in molecular homogenous catalysis along several decades. However, as also highlighted in the above sections, unravelling the exact role(s) of surface species in the observed catalytic output is still a challenge. The perceived effects are usually mixed and difficult to attribute to a single ligand contribution (i.e., electronic, steric, hydrophobic, etc.). Therefore, the full understanding of the role/fate of surface ligands under relevant conditions requires correlation studies involving catalyst benchmarking, cutting-edge operando characterization and realistic (experiment-based) multiscale[98–101] theoretical modeling. Catalyst benchmarking is relatively well stablished in electrocatalysis, but almost nonexistent in photo(electro)catalysis,[147,148] what hinders the meaningful comparison of light-driven systems and their ulterior rational improvement. This is a key general challenge that the community of researchers working in photo(electro)catalysis will need to urgently address. Also, exploiting the synergism between modeling (at different scales) and advanced surface-sensitive characterization techniques (i.e., ToF-SIMS,[78] TR-SERS,[102] etc.) is required to better comprehend central (and mostly unexplored) aspects such as ligand coordination modes (and their evolution under turnover conditions) and the dynamics of reaction intermediates[104] at the NPs surface. The implementation of computational methods at higher scales than conventional atomistic (DFT) modeling to guide surface functionalization in catalyst design remains also unexplored. The use of microkinetic methods[98] to identify critical reaction intermediates and rate-determining elementary reactions as well

as the use of fluid dynamics methods to consider real-life parameters of the employed cell/reactor is expected to positively impact the field and streamline catalyst (re)design.[150] The findings of this multidisciplinary approach will allow stablishing solid guidelines to rationally design the future generation of more efficient, selective, and fast nanoscale catalysts for AP.

Acknowledgements

G.M. and L.M. contributed equally to this work. Sustained support from MICINN, FEDER, AGAUR, CNRS, the University Paul Sabatier-Toulouse, and the IRN-HC3A Franco-Catalan action are gratefully acknowledged. Recent research projects and grants include PID2019-104171RB-I00-, PID2021-128197NA-I00, TED2021-129237B-I00, IDEX UNITI Emergence project (UFTMIP: 2015-209-CIF-d-DRD-127185), CTP2013-0016 and CTP2013-Midi-Pyrénées13053026. L.M. and G.M. acknowledge the UAB and MICINN for PIF and FPU predoctoral grants, respectively. L.F. is indebted to the Ramón y Cajal Program (RYC2018-025394-I Fellowship) and to the Royal Society of Chemistry (R20-8077 Research Fund). X.S thanks ICREA for the ICREA Academia prize 2020.

Conflict of Interest

The authors declare no conflict of interest.

Keywords

artificial photosynthesis, CO_2 reduction reaction, hydrogen evolution reaction, oxygen evolution reaction, surface-functionalized nanoparticles

Received: January 27, 2023
Revised: March 6, 2023
Published online: April 17, 2023

[1] G. Schmid, *Chem. Rev.* **1992**, *92*, 1709.
[2] G. Schmid, *Nanoparticles From Theory to Application*, 2nd ed. (Ed: G. Schmid), Wiley-VCH, New York **2010**.
[3] B. Corain, G. Schmid, N. Toshima, in *Metal Nanoclusters in Catalysis and Materials Science: The Issue of Size Control*, 1st ed. (Eds: B. Corain, G. Schmid, N. Toshima), Elsevier Science, Amsterdam **2008**.
[4] D. Astruc, *Chem. Rev.* **2020**, *120*, 461.
[5] In *Nanoparticles in Catalysis: Advances in Synthesis and Applications* (Eds: A. Rocoux, K. Philippot), Wiley-VCH, Weinheim **2021**.
[6] J. Zhu, L. Hu, P. Zhao, L. Y. S. Lee, K. Y. Wong, *Chem. Rev.* **2020**, *120*, 851.
[7] J. A. Trindell, Z. Duan, G. Henkelman, R. M. Crooks, *Chem. Rev.* **2020**, *120*, 814.
[8] L. Wu, Z. Xi, S. Sun, *Stud. Surf. Sci. Catal.* **2017**, *177*, 123.
[9] Q. Wang, K. Domen, *Chem. Rev.* **2020**, *120*, 919.
[10] F. H. Kaatz, A. Bultheel, *Nanoscale Res. Lett.* **2019**, *14*, 150.
[11] K. Zhou, Y. Li, *Angew. Chem., Int. Ed.* **2012**, *51*, 602.
[12] L. Lu, S. Zou, B. Fang, *ACS Catal.* **2021**, *11*, 6020.
[13] A. Heuer-Jungemann, N. Feliu, I. Bakaimi, M. Hamaly, A. Alkilany, I. Chakraborty, A. Masood, M. F. Casula, A. Kostopoulou, E. Oh, K. Susumu, M. H. Stewart, I. L. Medintz, E. Stratakis, W. J. Parak, A. G. Kanaras, *Chem. Rev.* **2019**, *119*, 4819.
[14] A. Dong, X. Ye, J. Chen, Y. Kang, T. Gordon, J. M. Kikkawa, C. B. Murray, *J. Am. Chem. Soc.* **2011**, *133*, 998.
[15] G. A. Somorjai, Y. Li, *Top. Catal.* **2010**, *53*, 311.
[16] N. S. Lewis, D. G. Nocera, *Proc. Natl. Acad. Sci. USA* **2006**, *103*, 15729.
[17] S. Berardi, S. Drouet, L. Francàs, C. Gimbert-Suriñach, M. Guttentag, C. Richmond, T. Stoll, A. Llobet, *Chem. Soc. Rev.* **2014**, *43*, 7501.
[18] X. Sala, S. Maji, R. Bofill, J. García-Antón, L. Escriche, A. Llobet, *Acc. Chem. Res.* **2014**, *47*, 504.
[19] J. Li, C. A. Triana, W. Wan, D. P. Adiyeri Saseendran, Y. Zhao, S. E. Balaghi, S. Heidari, G. R. Patzke, *Chem. Soc. Rev.* **2021**, *50*, 2444.
[20] R. Matheu, P. Garrido-Barros, M. Gil-Sepulcre, M. Z. Ertem, X. Sala, C. Gimbert-Suriñach, A. Llobet, *Nat. Rev. Chem.* **2019**, *3*, 331.
[21] M. Gil-Sepulcre, A. Llobet, *Nat. Catal.* **2022**, *5*, 79.
[22] N. Dubouis, A. Grimaud, *Chem. Sci.* **2019**, *10*, 9165.
[23] J. N. Hansen, H. Prats, K. K. Toudahl, N. Mørch Secher, K. Chan, J. Kibsgaard, I. Chorkendorff, *ACS Energy Lett.* **2021**, *6*, 1175.
[24] A. Zadick, L. Dubau, N. Sergent, G. Berthomé, M. Chatenet, *ACS Catal.* **2015**, *5*, 4819.
[25] D. Johnson, Z. Qiao, A. Djire, *ACS App. Energy Mater.* **2021**, *4*, 8661.
[26] Q. Lu, F. Jiao, *Nano Energy* **2016**, *29*, 439.
[27] J. R. Galan-Mascaros, *Catal. Sci. Technol.* **2020**, *10*, 1967.
[28] L. Francàs, S. Selim, S. Corby, D. Lee, C. A. Mesa, E. Pastor, K. S. Choi, J. R. Durrant, *Chem. Sci.* **2021**, *12*, 7442.
[29] R. Jin, Y. Pei, T. Tsukuda, *Acc. Chem. Res.* **2019**, *1*, 1.
[30] Y. Du, H. Sheng, D. Astruc, M. Zhu, *Chem. Rev.* **2020**, *120*, 526.
[31] B. L. Cushing, V. L. Kolesnichenko, C. J. O'Connor, *Chem. Rev.* **2004**, *104*, 3893.
[32] A. Roucoux, J. Schulz, H. Patin, *Chem. Rev.* **2002**, *102*, 3757.
[33] K. Philippot, B. Chaudret, *C. R. Chim.* **2003**, *6*, 1019.
[34] K. Philippot, B. Chaudret, in *Comprehensive Organometallic Chemistry III* (Eds: R. H. Crabtree, M. P. Mingos), Elsevier, Amsterdam **2007**, pp. 71–99.
[35] P. Lara, K. Philippot, L.-M. Lacroix, S. Lachaize, N. Liakakos, K. Soulantica, B. Chaudret, *Advances in Organometallic Chemistry and Catalysis*, John Wiley & Sons, Inc., New York **2013**, p. 421.
[36] C. Amiens, B. Chaudret, D. Ciuculescu-Pradines, V. Collière, K. Fajerwerg, P. Fau, M. Kahn, A. Maisonnat, K. Soulantica, K. Philippot, *New J. Chem.* **2013**, *37*, 3374.
[37] A. Denicourt-Nowicki, N. Mordvinova, A. Roucoux, in *Nanoparticles in Catalysis: Advances in Synthesis and Applications* (Eds: K. Philippot, A. Roucoux), Wiley, New York **2021**, p. 45.
[38] N. Toshima, T. Yonezawa, *New J. Chem.* **1998**, *22*, 1179.
[39] F. Fievet, S. Ammar-Merah, R. Brayner, F. Chau, M. Giraud, F. Mammeri, J. Peron, J. Y. Piquemal, L. Sicard, G. Viau, *Chem. Soc. Rev.* **2018**, *47*, 5187.
[40] U. Sanyal, B. R. Jagirdar, *Inorg. Chem.* **2012**, *51*, 13023.
[41] A. Meffre, S. Lachaize, C. Gatel, M. Respaud, B. Chaudret, *J. Mater. Chem.* **2011**, *21*, 13464.
[42] S. Scurti, E. Monti, E. Rodríguez-Aguado, D. Caretti, J. A. Cecilia, N. Dimitratos, *Nanomaterials* **2021**, *11*, 879.
[43] V. Sabadasch, S. Dachwitz, Y. Hannappel, T. Hellweg, N. Sewald, *Synthesis* **2022**, *54*, 3180.
[44] K. M. Koczkur, S. Mourdikoudis, L. Polavarapu, S. E. Skrabalak, *Dalton Trans.* **2015**, *44*, 17883.
[45] A. Denicourt-Nowicki, A. Roucoux, in *Metal Nanoparticles for Catalysis: Advances and Applications* (Ed: F. Tao), Royal Society of Chemistry, London **2014**, p. 99.
[46] L. S. Ott, R. G. Finke, *Coord. Chem. Rev.* **2007**, *251*, 1075.
[47] C. Amiens, D. Ciuculescu-Pradines, K. Philippot, *Coord. Chem. Rev.* **2016**, *308*, 409.
[48] M. R. Axet, K. Philippot, *Nanoparticles in Catalysis: Advances in Synthesis and Applications*, Wiley-VCH, Weinheim **2021**, p. 73.
[49] J. Muñoz, I. Álvarez-Prada, E. Lopez-Lopez, L. Escriche, N. Romero, X. Sala, M. Mas-Torrent, J. García-Antón, *Sens. Actuators, B* **2020**, *305*, 127467.

[50] M. Tasbihi, F. Fresno, I. Álvarez-Prada, A. Acharjya, A. Thomas, L. Escriche, N. Romero, X. Sala, V. A. de la Peña O'Shea, J. García-Antón, *J. CO2 Util.* **2021**, *50*, 101574.
[51] I. Álvarez-Prada, D. Peral, M. Song, J. Muñoz, N. Romero, L. Escriche, A. Acharjya, A. Thomas, R. Schomäcker, M. Schwarze, X. Sala, M. Tasbihi, J. García-Antón, *Renewable Energy* **2021**, *168*, 668.
[52] I. Álvarez-Prada, A. D. Nguyen, N. Romero, H. Hou, E. Benazzi, L. Escriche, A. Acharjya, A. Thomas, M. Schwarze, R. Schomäcker, X. Sala, M. Natali, J. García-Anto, M. Tasbihi, *Dalton Trans.* **2022**, *51*, 731.
[53] N. Romero, R. B. Guerra, L. Gil, S. Drouet, I. Salmeron-Sànchez, O. Illa, K. Philippot, M. Natali, J. García-Antón, X. Sala, *Sustainable Energy Fuels* **2020**, *4*, 4170.
[54] J. Creus, L. Mallón, N. Romero, R. Bofill, A. Moya, J. L. G. Fierro, R. Mas-Ballesté, X. Sala, K. Philippot, J. García-Antón, *Eur. J. Inorg. Chem.* **2019**, *2019*, 2071.
[55] Y. Zhao, J. R. Swierk, J. D. Megiatto, B. Sherman, W. J. Youngblood, D. Qin, D. M. Lentz, A. L. Moore, T. A. Moore, D. Gust, T. E. Mallouk, *Proc. Natl. Acad. Sci. USA* **2012**, *109*, 15612.
[56] J. de Tovar, N. Romero, S. A. Denisov, R. Bofill, C. Gimbert-Suriñach, D. Ciuculescu-Pradines, S. Drouet, A. Llobet, P. Lecante, V. Colliere, Z. Freixa, N. McClenaghan, C. Amiens, J. García-Antón, K. Philippot, X. Sala, *Mater. Today Energy* **2018**, *9*, 506.
[57] P. Sabatier, *Ber. Dtsch. Chem. Ges.* **1911**, *44*, 1984.
[58] H. Ooka, J. Huang, K. S. Exner, *Front. Energy Res.* **2021**, *9*, 654460.
[59] J. Rossmeisl, A. Logadottir, J. K. Nørskov, *Chem. Phys.* **2005**, *319*, 178.
[60] J. K. Nørskov, T. Bligaard, J. Rossmeisl, C. H. Christensen, *Nat. Chem.* **2009**, *1*, 37.
[61] J. Rossmeisl, Z. W. Qu, H. Zhu, G. J. Kroes, J. K. Nørskov, *J. Electroanal. Chem.* **2007**, *607*, 83.
[62] J. K. Nørskov, J. Rossmeisl, A. Logadottir, L. Lindqvist, J. R. Kitchin, T. Bligaard, H. Jónsson, *J. Phys. Chem. B* **2004**, *108*, 17886.
[63] S. Back, K. Tran, Z. W. Ulissi, *ACS Catal.* **2019**, *9*, 7651.
[64] Z. Li, L. E. K. Achenie, H. Xin, *ACS Catal.* **2020**, *10*, 4377.
[65] K. Broderick, E. Lopato, B. Wander, S. Bernhard, J. Kitchin, Z. Ulissi, *Appl. Catal., B* **2023**, *320*, 121959.
[66] S. Trasatti, *J. Electroanal. Chem. Interfacial Electrochem.* **1972**, *39*, 163.
[67] J. K. Nørskov, T. Bligaard, A. Logadottir, J. R. Kitchin, J. G. Chen, S. Pandelov, U. Stimming, *J. Electrochem. Soc.* **2005**, *152*, J23.
[68] T. F. Jaramillo, K. P. Jørgensen, J. Bonde, J. H. Nielsen, S. Horch, I. Chorkendorff, *Science* **2007**, *317*, 100.
[69] I. del Rosal, R. Poteau, *Nanoparticles in Catalysis*, Wiley, New York **2021**, p. 331.
[70] D. Eguchi, M. Sakamoto, T. Teranishi, *Chem. Sci.* **2018**, *9*, 261.
[71] Y. Peng, Q. Liu, B. Lu, T. He, F. Nichols, X. Hu, T. Huang, G. Huang, L. Guzman, Y. Ping, S. Chen, *ACS Catal.* **2021**, *11*, 1179.
[72] D. A. Henckel, O. Lenz, B. M. Cossairt, *ACS Catal.* **2017**, *7*, 2815.
[73] X. Wu, B. Feng, W. Li, Y. Niu, Y. Yu, S. Lu, C. Zhong, P. Liu, Z. Tian, L. Chen, W. Hu, C. M. Li, *Nano Energy* **2019**, *62*, 117.
[74] T. Li, O. Kasian, S. Cherevko, S. Zhang, S. Geiger, C. Scheu, P. Felfer, D. Raabe, B. Gault, K. J. J. Mayrhofer, *Nat. Catal.* **2018**, *1*, 300.
[75] L. Cusinato, L. M. Martínez-Prieto, B. Chaudret, I. Del Rosal, R. Poteau, *Nanoscale* **2016**, *8*, 10974.
[76] J. Creus, S. Drouet, S. Suriñach, P. Lecante, V. Collière, R. Poteau, K. Philippot, J. García-Antón, X. Sala, *ACS Catal.* **2018**, *8*, 11094.
[77] S. Drouet, J. Creus, V. Collière, C. Amiens, J. García-Antón, X. Sala, K. Philippot, *Chem. Commun.* **2017**, *53*, 11713.
[78] A. Atrei, B. Lesiak-Orlowska, J. Tóth, *Appl. Surf. Sci.* **2022**, *602*, 154366.
[79] L. Fan, B. Zhang, Z. Qiu, N. V. R. A. Dharanipragada, B. J. J. Timmer, F. Zhang, X. Sheng, T. Liu, Q. Meng, A. K. Inge, T. Edvinsson, L. Sun, *ChemSusChem* **2020**, *13*, 5901.
[80] B. Zhang, L. Sun, *Chem. Soc. Rev.* **2019**, *48*, 2216.
[81] D. R. Kauffman, D. R. Alfonso, D. N. Tafen, C. Wang, Y. Zhou, Y. Yu, J. W. Lekse, X. Deng, V. Espinoza, J. Trindell, O. K. Ranasingha, A. Roy, J. S. Lee, H. L. Xin, *J. Phys. Chem. C* **2018**, *122*, 27991.
[82] C. Kim, H. S. Jeon, T. Eom, M. S. Jee, H. Kim, C. M. Friend, B. K. Min, Y. J. Hwang, *J. Am. Chem. Soc.* **2015**, *137*, 13844.
[83] M. Gao, Y. Zhu, Y. Liu, K. Wu, H. Lu, S. Tang, C. Liu, H. Yue, B. Liang, J. Yan, *Chem. Commun.* **2020**, *56*, 7021.
[84] D. R. Kauffman, D. Alfonso, C. Matranga, H. Qian, R. Jin, *J. Am. Chem. Soc.* **2012**, *134*, 10237.
[85] Z. Wang, L. Wu, K. Sun, T. Chen, Z. Jiang, T. Cheng, W. A. Goddard, *J. Phys. Chem. Lett.* **2018**, *9*, 3057.
[86] Z. Wang, K. Sun, C. Liang, L. Wu, Z. Niu, J. Gao, *ACS Appl. Energy Mater.* **2019**, *2*, 192.
[87] C. Kim, T. Eom, M. S. Jee, H. Jung, H. Kim, B. K. Min, Y. J. Hwang, *ACS Catal.* **2017**, *7*, 779.
[88] L. Zhang, Z. Wei, S. Thanneeru, M. Meng, M. Kruzyk, G. Ung, B. Liu, J. He, *Angew. Chem.* **2019**, *131*, 15981.
[89] Z. Cao, D. Kim, D. Hong, Y. Yu, J. Xu, S. Lin, X. Wen, E. M. Nichols, K. Jeong, J. A. Reimer, P. Yang, C. J. Chang, *J. Am. Chem. Soc.* **2016**, *138*, 8120.
[90] M. R. Narouz, K. M. Osten, P. J. Unsworth, R. W. Y. Man, K. Salorinne, S. Takano, R. Tomihara, S. Kaappa, S. Malola, C. T. Dinh, J. D. Padmos, K. Ayoo, P. J. Garrett, M. Nambo, J. H. Horton, E. H. Sargent, H. Häkkinen, T. Tsukuda, C. M. Crudden, *Nat. Chem.* **2019**, *11*, 419.
[91] A. R. Riscoe, C. J. Wrasman, A. A. Herzing, A. S. Hoffman, A. Menon, A. Boubnov, M. Vargas, S. R. Bare, M. Cargnello, *Nat. Catal.* **2019**, *2*, 852.
[92] Q. Xiao, Y. Hu, Z. Liu, Z. Geng, F. Li, J. Zeng, *Nano Lett.* **2021**, *21*, 8924.
[93] T. C. Chou, C. C. Chang, H. L. Yu, W. Y. Yu, C. L. Dong, J. J. Velasco-Vélez, C. H. Chuang, L. C. Chen, J. F. Lee, J. M. Chen, H. L. Wu, *J. Am. Chem. Soc.* **2020**, *142*, 2857.
[94] W. Zhang, C. Huang, Q. Xiao, L. Yu, L. Shuai, P. An, J. Zhang, M. Qiu, Z. Ren, Y. Yu, *J. Am. Chem. Soc.* **2020**, *142*, 11417.
[95] Y. Zhou, F. Che, M. Liu, C. Zou, Z. Liang, P. De Luna, H. Yuan, J. Li, Z. Wang, H. Xie, H. Li, P. Chen, E. Bladt, R. Quintero-Bermudez, T.-K. Sham, S. Bals, J. Hofkens, D. Sinton, G. Chen, E. H. Sargent, *Nat. Chem.* **2018**, *10*, 974.
[96] H. Wu, J. Li, K. Qi, Y. Zhang, E. Petit, W. Wang, V. Flaud, N. Onofrio, B. Rebiere, L. Huang, C. Salameh, L. Lajaunie, P. Miele, D. Voiry, *Nat. Commun.* **2021**, *12*, 7210.
[97] Q. Chang, J. H. Lee, Y. Liu, Z. Xie, S. Hwang, N. S. Marinkovic, A. A. Park, S. Kattel, J. G. Chen, *J. Am. Chem. Soc.* **2022**, *2*, 214.
[98] A. H. Motagamwala, J. A. Dumesic, *Chem. Rev.* **2021**, *121*, 1049.
[99] Ž. Kovačič, B. Likozar, M. Huš, *ACS Catal.* **2020**, *10*, 14984.
[100] D. Kopač, B. Likozar, M. Huš, *ACS Catal.* **2020**, *10*, 4092.
[101] D. Ješić, D. Lašič Jurković, A. Pohar, L. Suhadolnik, B. Likozar, *Chem. Eng. J.* **2021**, *407*, 126799.
[102] H. An, L. Wu, L. D. B. Mandemaker, S. Yang, J. de Ruiter, J. H. J. Wijten, J. C. L. Janssens, T. Hartman, W. van der Stam, B. M. Weckhuysen, *Angew. Chem., Int. Ed.* **2021**, *60*, 16576.
[103] S. Zhao, O. Christensen, Z. Sun, H. Liang, A. Bagger, K. Torbensen, P. Nazari, J. V. Lauritsen, S. U. Pedersen, J. Rossmeisl, K. Daasbjerg, *Nat. Commun.* **2023**, *14*, 844.
[104] J. de Ruiter, H. An, L. Wu, Z. Gijsberg, S. Yang, T. Hartman, B. M. Weckhuysen, W. van der Stam, *J. Am. Chem. Soc.* **2022**, *144*, 15047.
[105] R. Zhang, P. E. Pearce, Y. Duan, N. Dubouis, T. Marchandier, A. Grimaud, *Chem. Mater.* **2019**, *31*, 8248.
[106] Y. J. Sa, C. W. Lee, S. Y. Lee, J. Na, U. Lee, Y. J. Hwang, *Chem. Soc. Rev.* **2020**, *49*, 6632.
[107] Y. Umena, K. Kawakami, J. R. Shen, N. Kamiya, *Nature* **2011**, *473*, 55.

[108] N. Kamiya, J. R. Shen, *Proc. Natl. Acad. Sci. USA* **2003**, *100*, 98.
[109] A. W. Nichols, C. W. Machan, *Front. Chem.* **2019**, *7*, 397.
[110] S. T. Stripp, B. R. Duffus, V. Fourmond, C. Léger, S. Leimkühler, S. Hirota, Y. Hu, A. Jasniewski, H. Ogata, M. W. Ribbe, *Chem. Rev.* **2022**, *122*, 11900.
[111] R. Matheu, M. Z. Ertem, C. Gimbert-Suriñach, X. Sala, A. Llobet, *Chem. Rev.* **2019**, *119*, 3453.
[112] M. Rakowski Du Bois, D. L. Du Bois, *Chem. Soc. Rev.* **2009**, *38*, 62.
[113] C. Costentin, S. Drouet, M. Robert, J.-M. Savéant, *Science* **2012**, *338*, 90.
[114] N. Vereshchuk, R. Matheu, J. Benet-Buchholz, M. Pipelier, J. Lebreton, D. Dubreuil, A. Tessier, C. Gimbert-surin, M. Z. Ertem, A. Llobet, C. Gimbert-Suriñach, M. Z. Ertem, A. Llobet, C. Gimbert-surin, M. Z. Ertem, A. Llobet, *J. Am. Chem. Soc.* **2020**, *142*, 5068.
[115] R. Matheu, M. Z. Ertem, J. Benet-buchholz, E. Coronado, V. S. Batista, X. Sala, A. Llobet, *J. Am. Chem. Soc.* **2015**, *137*, 10786.
[116] W. Li, F. Li, H. Yang, X. Wu, P. Zhang, Y. Shan, L. Sun, *Nat. Commun.* **2019**, *10*, 5074.
[117] L. Mallón, N. Romero, A. Jiménez, E. Martín Morales, J. Alemán, R. Mas-Ballesté, R. Bofill, K. Philippot, J. García-Antón, X. Sala, *Catal. Sci. Technol.* **2020**, *10*, 4513.
[118] X. Han, L. Liu, J. Yuan, X. Zhang, D. Niu, *ChemSusChem* **2021**, *14*, 721.
[119] J. R. Pankhurst, P. Iyengar, V. Okatenko, R. Buonsanti, *Inorg. Chem.* **2021**, *60*, 6939.
[120] J. R. Pankhurst, Y. T. Guntern, M. Mensi, R. Buonsanti, *Chem. Sci.* **2019**, *10*, 10356.
[121] L. Ma, W. Hu, Q. Pan, L. Zou, Z. Zou, K. Wen, H. Yang, *J. CO2 Util.* **2019**, *34*, 108.
[122] D. Alba-Molina, A. R. Puente Santiago, J. J. Giner-Casares, E. Rodríguez-Castellón, M. T. Martín-Romero, L. Camacho, R. Luque, M. Cano, *J. Mater. Chem. A: Mater.* **2019**, *7*, 20425.
[123] D. Ung, B. M. Cossairt, *ACS Appl. Energy Mater.* **2019**, *2*, 1642.
[124] Q. Guo, T. Lan, Z. Su, F. Zheng, W. Chen, *Mater. Rep.: Energy* **2022**, *3*, 100172.
[125] Q. Zhu, C. J. Murphy, L. R. Baker, *J. Am. Chem. Soc.* **2022**, *144*, 2829.
[126] D. R. Kauffman, P. R. Ohodnicki, B. W. Kail, C. Matranga, *J. Phys. Chem. Lett.* **2011**, *2*, 2038.
[127] Y. Zhao, C. Wang, Y. Liu, D. R. MacFarlane, G. G. Wallace, *Adv. Energy Mater.* **2018**, *8*, 1801400.
[128] H. Shang, S. K. Wallentine, D. M. Hofmann, Q. Zhu, C. J. Murphy, L. R. Baker, *Chem. Sci.* **2020**, *11*, 12298.
[129] J. R. Pankhurst, P. Iyengar, A. Loiudice, M. Mensi, R. Buonsanti, *Chem. Sci.* **2020**, *11*, 9296.
[130] D. Kim, S. Yu, F. Zheng, I. Roh, Y. Li, S. Louisia, Z. Qi, G. A. Somorjai, H. Frei, L.-W. Wang, P. Yang, *Nat. Energy* **2020**, *5*, 1032.
[131] S. Yu, D. Kim, Z. Qi, S. Louisia, Y. Li, G. A. Somorjai, P. Yang, *J. Am. Chem. Soc.* **2021**, *143*, 19919.
[132] L. Liu, X. Zhang, L. Yang, L. Ren, D. Wang, J. Ye, *Nat. Sci. Rev.* **2017**, *4*, 761.
[133] H. Nasrallah, F. Douma, H. I. Hamoud, M. El-Roz, *Nanostructured Photocatalysts: From Fundamental to Practical Applications*, Elsevier, Amsterdam **2021**, p. 119.
[134] R. Godin, A. Kafizas, J. R. Durrant, *Curr. Opinion Electrochem.* **2017**, *2*, 136.
[135] S. Corby, R. R. Rao, L. Steier, J. R. Durrant, *Nat. Res.* **2021**, *6*, 1136.
[136] A. Reynal, J. Willkomm, N. M. Muresan, F. Lakadamyali, M. Planells, E. Reisner, J. R. Durrant, *Chem. Commun.* **2014**, *50*, 12768.
[137] S. Jeong, G. M. Kim, G. S. Kang, C. Kim, H. Lee, W. J. Kim, Y. K. Lee, S. Lee, H. Kim, H. K. Lim, D. C. Lee, *J. Phys. Chem. C* **2019**, *123*, 29184.
[138] Q. T. Nguyen, E. Rousset, V. T. H. Nguyen, V. Colliere, P. Lecante, W. Klysubun, K. Philippot, J. Esvan, M. Respaud, G. Lemercier, P. D. Tran, C. Amiens, *ACS Appl. Mater. Interfaces* **2021**, *13*, 53829.
[139] P. G. Hoertz, Y. il Kim, W. J. Youngblood, T. E. Mallouk, *J. Phys. Chem. B* **2007**, *111*, 6845.
[140] E. Martín Morales, Y. Coppel, P. Lecante, I. del Rosal, R. Poteau, J. Esvan, P. Sutra, K. Philippot, A. Igau, *Chem. Commun.* **2020**, *56*, 4059.
[141] W. J. Youngblood, S. A. Lee, Y. Kobayashi, E. A. Hernandez-pagan, P. G. Hoertz, T. A. Moore, A. L. Moore, D. Gust, T. E. Mallouk, *J. Am. Chem. Soc.* **2009**, *131*, 926.
[142] M. G. Lee, K. Jin, K. C. Kwon, W. Sohn, H. Park, K. S. Choi, Y. K. Go, H. Seo, J. S. Hong, K. T. Nam, H. W. Jang, *Adv. Sci.* **2018**, *5*, 1800727.
[143] P. Wang, J. Zhang, H. He, X. Xu, Y. Jin, *Nanoscale* **2015**, *7*, 5767.
[144] Y. Ben-Shahar, F. Scotognella, N. Waiskopf, I. Kriegel, S. Dal Conte, G. Cerullo, U. Banin, *Small* **2015**, *11*, 462.
[145] D. A. Hines, P. V. Kamat, *ACS Appl. Mater. Interfaces* **2014**, *6*, 3041.
[146] G.-L. Hu, R. Hu, Z.-H. Liu, K. Wang, X.-Y. Yan, H.-Y. Wang, *Catal. Sci. Technol.* **2020**, *10*, 5677.
[147] M. Melchionna, P. Fornasiero, *ACS Catal.* **2020**, *10*, 5493.
[148] P. v. Kamat, S. Jin, *ACS Energy Lett.* **2018**, *3*, 622.
[149] Y. Zhou, A. J. Martín, F. Dattila, S. Xi, N. López, J. Pérez-Ramírez, B. S. Yeo, *Nat. Catal.* **2022**, *5*, 545.
[150] X. Zhang, Z. Zhou, *J. Phys. Chem. C* **2022**, *126*, 3820.

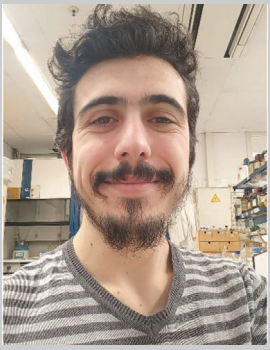

Gerard Martí is a Ph.D. student from the Material Science Ph.D. program from Universitat Autònoma de Barcelona who joined the SelOxCat research group in 2019 starting as an undergraduate student. During this time, he has been working on the synthesis and characterization of metal and metal-oxide nanoparticles, such Ru, Cu, Ni, Pt, and Au. These nanoparticles have applications on electro and photocatalysis, in this case he uses them for the generation of hydrogen from water and CO_2 transformation to value added products.

Laura Mallón joined the SeloxCat research group as undergraduate student in 2015, working since that time on the synthesis, characterization, theoretical modelling, and catalytic properties of colloidal and supported nanoparticulated, Ru, Ni, and Co-based catalysts for their application in the oxygen and hydrogen evolution reactions. She obtained her PhD in Chemistry in 2021, under a cotutelle agreement between Universitat Autònoma de Barcelona (UAB) and Université Toulouse III – Paul Sabatier.

Nuria Romero obtained her Ph.D. degree in organometallic chemistry of Early Transition Metals in 2014 from Université Paul Sabatier-Toulouse III/Laboratoire de Chimie de Coordination-CNRS in France. She realized a postdoctoral stay of 18 months at the Université de Rennes 1 (France) in collaboration with Total Energies working on olefin polymerization. She was postdoctoral researcher for 5 years at the Universitat Autònoma de Barcelona (Spain) where she started developing catalysts for artificial photosynthesis. After a postdoctoral stay at Laboratoire de Chimie de Coordination-CNRS working on alkaline electrolysis, she became associate professor at Université Paul Sabatier-Toulouse III in 2022.

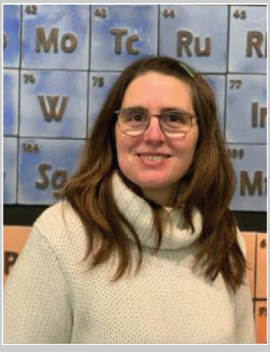

Laia Francàs obtained her Ph.D. in Chemistry at Universitat Autònoma de Barcelona (UAB) in 2011. After, she did two postdoctoral stays: the first one at the Institute of Chemical Research of Catalonia (ICIQ, 2011–2014); and her second one at Imperial College London (2015–2018). Since 2020, she has returned to the UAB as an independent researcher at SelOxCat group, thanks to a Ramon y Cajal contract. Currently she is leading the projects devoted to the design of ligand functionalized (photo)electrodes for solar fuels applications to study their activity, properties, and mechanism by means of electrochemistry and UV–vis spectroelectrochemistry.

Roger Bofill obtained his Ph.D. in Chemistry at the Universitat Autònoma de Barcelona (UAB) in 2001. He was a post-doctoral fellow at the School of Biological Sciences, University of Sussex (Oct. 2001–June 2002), and at the Centre for Biomolecular Sciences, University of Nottingham (July 2002–July 2004). He then rejoined the UAB as a lecturer and researcher, obtaining his tenure in 2009. In 2012, he joined the SelOxCat research group, working on the synthesis and catalytic properties of molecular and nanoparticulated Ru and Co-based catalysts for their application in the water oxidation and the proton and CO_2 reduction reactions.

Karine Philippot received her Ph.D. degree in Molecular Chemistry and Catalysis in 1993 and her habilitation in 2007 from the University Paul Sabatier-Toulouse. She has been a CNRS Researcher at the LCC- Toulouse since 1996 and the head of the group "Engineering of Metal Nanoparticles" since 2008. She develops the synthesis of metal nanoparticles and composite nanomaterials by using molecular chemistry concepts, for their application in catalysis and energy. She coedited 2 books in the domain of nanocatalysis: "Nanomaterials in Catalysis" and "Nanoparticles in Catalysis: Advances in Synthesis and Applications" (2013 and 2021, Wiley-VCH).

Jordi García-Antón received his Ph.D. in Chemistry in 2003 from the Universitat Autònoma de Barcelona (UAB). Then, he pursued a postdoctoral stay at the Laboratoire de Chimie de Coordination (Dr. Chaudret group; Toulouse, France), where his work dealt with the synthesis and characterization of metallic nanoparticles and the study of their surface coordination chemistry. In 2006, Dr. García-Antón joined the UAB as a lecturer in chemistry and in 2014 he became an associate professor. His research interest focuses on the preparation of metallic or metal-oxide nanoparticles through the organometallic approach and their use as (photo)catalysts in artificial photosynthesis processes.

Xavier Sala received his Ph.D. in Chemistry from the University of Girona in 2007. He conducted postdoctoral research with P. W. N. M. van Leeuwen and A. Llobet at the Catalan Institute of Chemical Research of Catalonia (ICIQ, 2007–2010). In 2010, he was appointed Lecturer at the Autonomous University of Barcelona (UAB) and then promoted to associate professor in 2018. Since 2011, he leads the "Selective Redox Catalysis" (SelOxCat) research group at UAB, focused on the study, comprehension and development of the key catalytic processes involved in the production of solar fuels through artificial photosynthesis.